

1           **A computational framework for time dependent**  
2           **deformation in viscoelastic magmatic systems**

3           **Cody Rucker (crucker@uoregon.edu)<sup>1</sup>, Brittany A. Erickson**  
4           **(bae@uoregon.edu)<sup>1,2</sup>, Leif Karlstrom (leif@uoregon.edu)<sup>2</sup>, Brian Lee**  
5           **(bl7@pdx.edu)<sup>3</sup>, and Jay Gopalakrishnan (gjay@pdx.edu)<sup>3</sup>**

6           <sup>1</sup>Department of Computer and Information Science, University of Oregon, Eugene, OR, USA

7                   <sup>2</sup>Department of Earth Sciences, University of Oregon, Eugene, OR, USA

8           <sup>3</sup>Department of Mathematics and Statistics, Portland State University, Portland, OR, USA

9           This manuscript has been submitted for publication in the Journal of Geophys-  
10          ical Research: Solid Earth. Please note that, despite having undergone peer-review, the  
11          manuscript has yet to be formally accepted for publication. Subsequent versions of this  
12          manuscript may have slightly different content. If accepted, the final version of this manuscript  
13          will be available via the 'Peer-reviewed Publication DOI' link on the right-hand side of  
14          this webpage. Please feel free to contact any of the authors; we welcome feedback.

---

Corresponding author: Cody Rucker, [crucker@uoregon.edu](mailto:crucker@uoregon.edu)

15

**Key Points:**

16

- A high-order numerical framework is derived for time-dependent viscoelastic deformation around magma reservoirs.

17

18

- The transfer function characterizes phase lag and amplification between pressurization at depth and surface deformation.

19

20

- The spatial extent of viscous response is frequency dependent and well-characterized by a local Deborah number.

21

**Abstract**

Time-dependent ground deformation is a key observable in magmatic systems, but is challenging to characterize. Here we present a numerical framework for modeling transient deformation and stress around a subsurface, spheroidal pressurized magma reservoir within a viscoelastic half-space with variable material coefficients, utilizing a high-order finite-element method and explicit time-stepping. We derive numerically stable time steps and verify convergence, then explore the frequency dependence of surface displacement associated with cyclic pressure applied to a spherical reservoir beneath a stress-free surface. We consider a Maxwell rheology and a steady geothermal gradient, which gives rise to spatially variable viscoelastic material properties. The temporal response of the system is quantified with a transfer function that connects peak surface deformation to reservoir pressurization in the frequency domain. The amplitude and phase of this transfer function characterize the viscoelastic response of the system, and imply a framework for characterizing general deformation timeseries through superposition. Transfer function components vary with the frequency of pressure forcing and are modulated strongly by the background temperature field. The dominantly viscous region around the reservoir is also frequency dependent, through a local Deborah number that measures pressurization period against a spatially varying Maxwell relaxation time. This near-reservoir region defines a spatially complex viscous/elastic transition whose volume depends on the frequency of forcing. Our computational and transfer function analysis framework represents a general approach for studying transient viscoelastic crustal response to magmatic forcing through spectral decomposition of deformation timeseries, such as long-duration geodetic observations.

**Plain Language Summary**

Ground motions associated with subsurface magma reservoirs are the result both of magma movement and time-dependent deformation of crustal rocks. We have developed a new computational framework to help interpret surface deformations associated with magmatic systems embedded within viscoelastic rocks as expected in volcanic regions. This framework is general in the sense that a broad range of scientific studies can be explored by specifying particular conditions at domain boundaries or magma reservoir geometries, and we perform rigorous numerical tests to ensure credible solutions. We then apply the model to study a simple but highly generalizable type of transient behavior - the cyclic pressurization and depressurization of a spherical reservoir. We develop a theoretical approach to simply analyze the time-dependent output, and find that temporal lag and amplification of surface deformation with respect to the reservoir pres-

57 sure is explained by an aureole of material surrounding the chamber with a dominantly  
58 viscous response, whose size is frequency-dependent. Our results can be extended to many  
59 transient deformation scenarios because a sinusoidal response forms the basic element  
60 of general pressure time-series.

## 61 **1 Introduction**

62 Magma reservoirs represent a fundamental link between mantle melting and vol-  
63 canic activity seen at the surface. Eruptions that drain these reservoirs are the most dra-  
64 matic example of magma chamber mechanics, but a wide spectrum of time-varying sur-  
65 face deformation and other unrest seen in volcanic regions likely has an origin within crustal  
66 storage zones (Anderson & Segall, 2011; Cianetti et al., 2012; Henderson & Pritchard,  
67 2017; Walwer et al., 2021). As a result, understanding controls on time-dependent magma  
68 chamber deformation and stress is a long-standing research topic in volcanology (Sparks  
69 et al., 2017; Segall, 2019). However, modeling magma reservoir evolution is a challeng-  
70 ing problem because time-dependence may arise from a variety of physical processes oc-  
71 ccurring both internal and external to the magma transport system, many of which leave  
72 non-unique signatures in ground deformation patterns.

73 On sufficiently short time scales, it is appropriate to assume an elastic/brittle rhe-  
74 ology of host rocks. Elastic models have been widely used to interpret geodetic data gath-  
75 ered at volcanoes (Mogi, 1958; McTigue, 1987; Berrino et al., 1984). Such models pre-  
76 dict that time-dependent behavior comes only from reservoir magma mass balance/state  
77 variable changes (Cianetti et al., 2012) or boundary forcing, although poroelastic effects  
78 can also lead to time-dependence (Mittal & Richards, 2019). Time dependent deforma-  
79 tion and stressing of the reservoir at longer timescales likely involves ductile response of  
80 host rocks (e.g., Gottsmann & Odbert, 2014; Yamasaki et al., 2018; Novoa et al., 2019),  
81 suggesting an overall viscoelastic rheology.

82 Viscoelastic effects have been identified as defining a notion of magma chamber sta-  
83 bility, providing a mechanism for modulating stresses and deformation associated with  
84 pressurization of the chamber (Dragoni & Magnanensi, 1989; Karlstrom et al., 2010; Gregg  
85 et al., 2013; Liao et al., 2021). Viscoelastic effects may play a role in the development  
86 of large silicic reservoirs (Jellinek & DePaolo, 2003) as well as eruption sequences from  
87 long-lived magma reservoirs (Degruyter & Huber, 2014) and time-dependent ground de-  
88 formation at active volcanoes in diverse settings (Newman et al., 2001; Sigmundsson et  
89 al., 2010; Masterlark et al., 2010; Le Mével et al., 2016; Morales Rivera et al., 2019). On  
90 tectonic timescales, state shifts in the magma transport system reflected by increasing

91 intrusive-extrusive ratios, and evolving spatial organization of volcanic output around  
92 spatial centers, may also reflect time-evolving viscoelastic behavior (Karlstrom et al., 2017).

93 Deformation style is strongly tied to the thermal state of the magmatic system, be-  
94 cause both rock and magma rheology are temperature dependent. Thus it is to be ex-  
95 pected that a viscoelastic response varies spatially, and evolves in time with the tran-  
96 s-crustal magma transport system. Such unsteady effects, both spatial and temporal, are  
97 poorly constrained. Instead it is typically assumed that magma reservoirs reside in a steady  
98 state geotherm (Del Negro et al., 2009; Gregg et al., 2012; Head et al., 2021), or that the  
99 mechanical response is well-approximated by a pre-specified shell of viscous material in  
100 an elastic host (Bonafede et al., 1986; Karlstrom et al., 2010; Degruyter & Huber, 2014;  
101 Segall, 2016; Townsend et al., 2019). Time evolution is often either imposed kinemat-  
102 ically through stress boundary conditions (e.g., to model an eruptive event, (Dragoni &  
103 Magnanensi, 1989)) or arises dynamically through mass and energy balance (e.g., Karl-  
104 strom et al., 2010). Viscous creep independent of time-variable forcing has also been in-  
105 voked to explain deformation signals (Segall, 2016; Head et al., 2019), but general time  
106 dependent deformation has not been studied.

107 In this work, we address two aspects of viscoelastic deformation in magmatic sys-  
108 tems. First, we derive and implement a high order numerical modeling framework for  
109 simulating transient thermo-mechanical behavior of a subsurface magma reservoir in an  
110 isotropic, heterogeneous, viscoelastic domain. Second, we study stress and crustal de-  
111 formation associated with periodic pressure variation at the chamber wall. This repre-  
112 sents a different sort of idealization than previous studies: we consider spatially resolved  
113 mechanical response, but treat time evolution as harmonic. In this way we isolate the  
114 frequency dependence of the viscoelastic rheology, and develop a transfer function ap-  
115 proach using analytic functions to predict material response. This idealization might ap-  
116 proximate some magmatic forcing scenarios, such as cyclic stress from seismic waves, pe-  
117 riodic magma injection, or glacial cycles, and we note that quasi-periodic deformation  
118 at multiple frequencies has been observed in long-term geodetic timeseries (Crozier &  
119 Karlstrom, 2022). But this approach also implies a superposition framework for study-  
120 ing much more general time evolution.

121 Our model is developed to handle general axisymmetric geometries in the subsur-  
122 face and surface, including lateral loads and topographically complex material interfaces.  
123 However, we focus on the relatively simple and well-studied case of a sphere in a half-  
124 space without remote loading to explore transient effects, deriving material properties  
125 from a steady state temperature distribution within the medium. After detailing the nu-  
126 merical framework we verify convergence using the method of manufactured solutions

127 (Roache, 1998). Finally we use the verified framework to characterize the system’s  
 128 response to spatially variable viscoelastic material properties. We develop a transfer func-  
 129 tion between chamber pressure and maximum vertical surface deformation to demon-  
 130 strate that two parameters – the phase lag between pressurization and surface deforma-  
 131 tion, and their relative amplitude – imply a frequency-dependent viscoelastic response  
 132 that depends on chamber temperature and geothermal gradient magnitude. We demon-  
 133 strate that this transfer function permits the reconstruction of complex deformation his-  
 134 tories, and show that the spatial thermo-rheologic structure beneath the chamber influ-  
 135 ences frequency-domain expression of surface deformation.

136 The paper is organized with mathematical and computational details provided first,  
 137 followed by the spectral (and transfer function) analysis and example calculations. In  
 138 Section 2 we introduce the governing equations and generic physical problem of inter-  
 139 est. In Section 3 we discuss the computational framework for solving our problem, sta-  
 140 bility considerations and resolution tests, and develop the specific non-dimensional time-  
 141 dependent problem of interest. Readers wishing to skip such technical details can go di-  
 142 rectly to section 4, which introduces the transfer function approach that represents our  
 143 primary analysis tool. Section 5 then discusses results of computations and Section 6 dis-  
 144 cusses implications for magmatic systems.

## 145 **2 Mathematical Framework**

### 146 **2.1 Problem Formulation and Geometry**

147 We consider a subsurface magma reservoir in an isotropic, viscoelastic space, see  
 148 Figure 1. In general the system evolves in time in response to mass, momentum, and en-  
 149 ergy balance associated with magma transport in and out of the reservoir. We focus here  
 150 on the host response to one particular state variable, a uniform but time-evolving pres-  
 151 sure on the reservoir wall.

152 We employ a cylindrical coordinate system  $(r, z, \theta)$  with the origin at the reservoir  
 153 center. The assumption of axisymmetry means the problem shows no variation along the  
 154  $\theta$ -coordinate enabling solutions in the one-sided  $(r, z)$ -plane. Figure 1 illustrates the  
 155 geometry which defines the computational region surrounding a reservoir. The magma  
 156 cavity has horizontal axis  $a > 0$  and vertical axis  $b > 0$ , with center at the origin, and  
 157 Earth’s free surface at  $z = D + b$  ( $z$  positive upwards). Maximum depth of the com-  
 158 putational domain is denoted by  $L_z$  and the maximum lateral distance from the center  
 159 of radial symmetry is denoted by  $L_r$ .

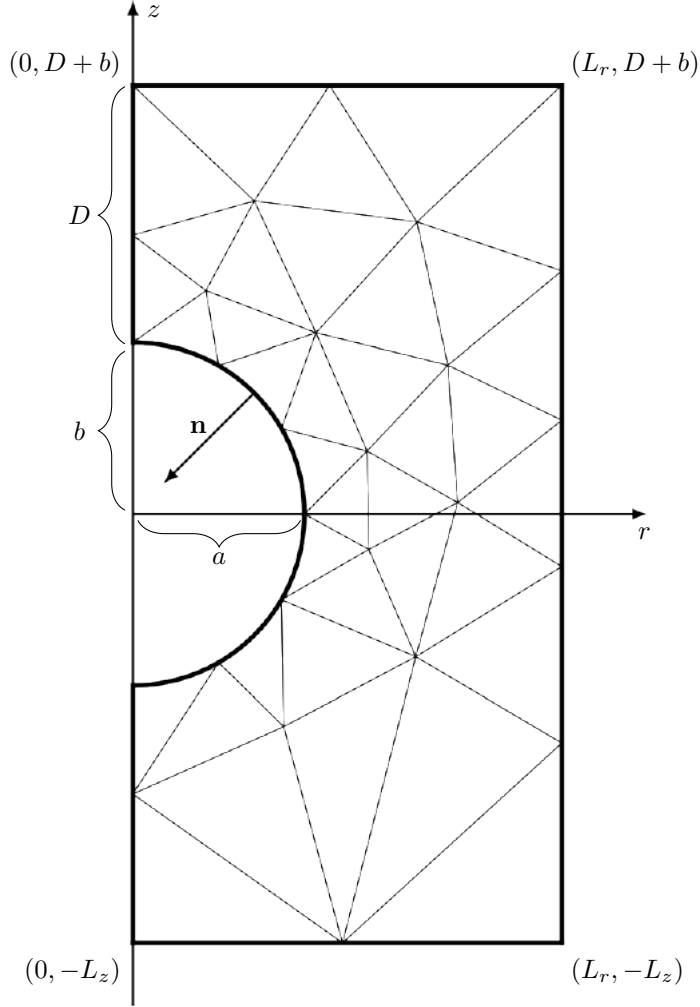


**Figure 1.** The region  $\Omega$  outside a subsurface, spheroidal magma reservoir centered at the origin is discretized with a high-order FEM. The reservoir has a horizontal axis  $a > 0$  and vertical axis  $b > 0$ . The distance from the top of the reservoir to the surface is  $D > b$ . The region is bounded by a maximal depth  $L_z$  and maximal distance from the radial center  $L_r$ . Though an example triangulation of the domain is shown, actual simulations are performed on a finer grid of points.

160 We construct the region outside of the cavity by intersecting a closed, rectangular  
 161 region  $\mathcal{D} = \{(r, z) \in \mathbb{R}^2 \mid 0 < r < L_r, -L_z < z < D + b\}$  and a punctured do-  
 162 main  $\mathcal{B} = \{(r, z) \in \mathbb{R}^2 \mid \frac{r^2}{a^2} + \frac{z^2}{b^2} > 1\}$ . The region  $\Omega$  outside of the cavity, defined  
 163 by  $\Omega = \mathcal{D} \cap \mathcal{B}$  forms our two-dimensional computational domain. The physical three-  
 164 dimensional problem is posed on the revolution of  $\Omega$ , the three-dimensional domain we  
 165 denote by  $\check{\Omega}$ .

## 166 2.2 Governing Equations

167 We assume sufficiently slow deformation so that quasi-static viscoelasticity is a valid  
 168 description of the momentum balance. We assume the medium deforms according to the  
 169 Maxwell constitutive law (Muki & Sternberg, 1961). This material model is chosen for  
 170 its simplicity and flexibility. A variety of linear and nonlinear viscoelastic models have  
 171 been proposed for crustal rocks at high temperature; the Maxwell model is a useful and  
 172 easily generalizable reference case for understanding the phenomenology of viscoelastic  
 173 deformation (Lau et al., 2020; Head et al., 2021).

174 Let  $\mathbf{u}, \underline{\boldsymbol{\varepsilon}}, \underline{\boldsymbol{\gamma}}, \underline{\boldsymbol{\sigma}}$  be, respectively, the displacement vector, the total strain tensor, the  
 175 viscous strain tensor, and the stress tensor. The time derivative of  $\underline{\boldsymbol{\gamma}}$  is denoted by  $\dot{\underline{\boldsymbol{\gamma}}}$ .  
 176 The relevant governing equations are:

$$177 \quad \operatorname{div} \underline{\boldsymbol{\sigma}} = \mathbf{f} \quad \text{in } \check{\Omega}, \quad (1a)$$

$$178 \quad \dot{\underline{\boldsymbol{\gamma}}} = \mathbf{A} \underline{\boldsymbol{\sigma}} \quad \text{in } \check{\Omega}, \quad (1b)$$

$$179 \quad \underline{\boldsymbol{\sigma}} = \mathbf{E}(\underline{\boldsymbol{\varepsilon}}(\mathbf{u}) - \underline{\boldsymbol{\gamma}}) \quad \text{in } \check{\Omega}, \quad (1c)$$

180 where  $\underline{\boldsymbol{\varepsilon}}(\mathbf{u}) = (\nabla \mathbf{u} + \nabla \mathbf{u}^T)/2$ ,  $\mathbf{E}$  is the fourth-order, isotropic elastic stiffness tensor  
 181 whose  $(i, j, k, l)$ -component in Cartesian coordinates is given by

$$182 \quad E_{ijkl} = \lambda \delta_{ij} \delta_{kl} + \mu (\delta_{ik} \delta_{jl} + \delta_{il} \delta_{jk}). \quad (2)$$

183 Here,  $\mu$  denotes the shear modulus,  $\lambda$  denotes Lamé's first parameter, and  $\delta$  denotes the  
 184 components of the identity tensor. The fourth-order tensor  $\mathbf{A}$  relates viscous strain to  
 185 stress, and is derived from the Maxwell constitutive law (Muki & Sternberg, 1961) to pro-  
 186 duce the form

$$187 \quad \mathbf{A} \underline{\boldsymbol{\sigma}} = \frac{1}{2\eta} \left( \sigma_{ij} - \frac{1}{3} \sigma_{kk} \delta_{ij} \right), \quad (3)$$

188 where  $\eta$  denotes the viscosity and repeated indices indicate summation over that index.

189 Equation (1a) is the static equilibrium equation where  $\mathbf{f}$  represents body forces.  
 190 Equation (1b) is the aging law for a Maxwell material and Equation (1c) is Hooke's Law.  
 191 When supplemented by initial and boundary conditions, the system (1a) can be solved  
 192 in any coordinate system.



193 We use the cylindrical coordinate system  $(r, z, \theta)$ , writing the displacement vector  
 194 field as  $\mathbf{u} = u_r \mathbf{e}_r + u_z \mathbf{e}_z + u_\theta \mathbf{e}_\theta$  where  $\mathbf{e}_r, \mathbf{e}_\theta$ , and  $\mathbf{e}_z$  denote the unit vectors of the  
 195 cylindrical coordinate system. The source  $\mathbf{f}$  can also be similarly expressed. We assume  
 196 that  $u_\theta$  and  $f_\theta$  are zero. Furthermore, by the assumption of axial symmetry,  $u_r$  and  $u_z$   
 197 are independent of  $\theta$ . Hence, employing the cylindrical components of the strain tensor,  
 198 displacements in the Earth are related to strains by

$$199 \quad \underline{\boldsymbol{\varepsilon}}(\mathbf{u}) = \frac{u_r}{r} \mathbf{e}_\theta \otimes \mathbf{e}_\theta + \sum_{i,j \in \{r,z\}} \frac{1}{2} (\partial_i u_j + \partial_j u_i) \mathbf{e}_i \otimes \mathbf{e}_j. \quad (4)$$

200 The stress tensor can be expressed, omitting its zero components, as

$$201 \quad \underline{\boldsymbol{\sigma}} = \sigma_{\theta\theta} \mathbf{e}_\theta \otimes \mathbf{e}_\theta + \sum_{i,j \in \{r,z\}} \sigma_{ij} \mathbf{e}_i \otimes \mathbf{e}_j. \quad (5)$$

202 The equilibrium equation (1a) then takes the form

$$203 \quad \left( \partial_r \sigma_{rr} + \partial_z \sigma_{rz} + \frac{1}{r} (\sigma_{rr} - \sigma_{\theta\theta}) \right) \mathbf{e}_r + \left( \partial_r \sigma_{rz} + \partial_z \sigma_{zz} + \frac{1}{r} \sigma_{rz} \right) \mathbf{e}_z = \mathbf{f}. \quad (6)$$

204 Using (4) and (1c) to obtain expressions for the cylindrical components of the stress ten-  
 205 sor, the equilibrium equation (6) can be solved for the components of the displacement  
 206 in the two-dimensional meridian  $(rz)$  plane.

207 To reduce the problem to the meridian half-plane where  $r > 0$ , we need to im-  
 208 pose the following boundary conditions on the axial boundary  $\Gamma_0 = \{(r, z) \in \partial\Omega : r = 0\}$ , namely

$$210 \quad u_r = 0, \quad \text{on } \Gamma_0 \quad (7a)$$

$$211 \quad \sigma_{rz} = 0, \quad \text{on } \Gamma_0. \quad (7b)$$

212 The first follows from a “no-opening” condition at  $r = 0$ . The second comes from re-  
 213 quiring continuity of stresses in the  $\mathbf{e}_z$  direction at  $r = 0$ . Other boundary conditions  
 214 are imposed by partitioning the remaining boundary  $\partial\Omega \setminus \Gamma_0$ . We let  $\Gamma_{\text{disp}} \subseteq \partial\Omega$  and  
 215  $\Gamma_{\text{trac}} = \partial\Omega \setminus \Gamma_{\text{disp}}$  denote a general partitioning of  $\partial\Omega$  into subdomains where either  
 216 displacement or traction boundary conditions are imposed, respectively. Explicitly, these  
 217 conditions are

$$218 \quad \mathbf{u} = \mathbf{g}_{\text{disp}}(t) \quad \text{on } \Gamma_{\text{disp}}, \quad (7c)$$

$$219 \quad \underline{\boldsymbol{\sigma}} \cdot \mathbf{n} = \mathbf{g}_{\text{trac}}(t) \quad \text{on } \Gamma_{\text{trac}}, \quad (7d)$$

220 where  $\mathbf{n}$  is the outward unit normal to the domain  $\Omega$ , and  $\mathbf{g}_{\text{disp}}, \mathbf{g}_{\text{trac}}(t)$  are given, time-  
 221 varying boundary data. This general model enables the study of reservoir pressure, lat-  
 222 eral loads and topography, among other studies in axisymmetric geometries.

In addition to boundary conditions, we must also supplement the aging law, Equation (1b), with an initial condition on viscous strain, namely

$$\underline{\gamma}(r, z, t = 0) = \underline{\gamma}_0(r, z), \quad (r, z) \in \Omega. \quad (8)$$

### 3 Computational Framework

We solve initial-boundary-value problem (Equations (1a),(4)-(8)) numerically by pairing a finite difference discretization in time with a high-order finite element method (FEM) in space. As described in this section, at each time step the spatial problem is governed by static equilibrium, with viscous effects manifested as a time-dependent source term. Simulations are done using Python code developed on top of the free and open source multi-physics library NGSolve (Schöberl, 2010–2022) and the accompanying mesh generator (Schöberl, 1997). The Python code is available in a public repository (*Bitbucket: magmaxisym*, 2022). We use a two-dimensional mesh of triangles. To capture the magma chamber boundary accurately, we use nonlinear mappings for those elements with edges on the curved boundary to improve geometrical conformity (Ern & Guermond, 2021). The following subsections outline the static problem, the temporal discretization, and the details of the specific problem considered in this work.

#### 3.1 Solving the Static Equilibrium Equation

We solve the equilibrium equations (1a) subject to boundary conditions (7) using a FEM, which requires the weak form of the problem. To construct the weak form, we perform the following steps: (i) multiply equation (6) by  $r$  and take the dot product of both sides with a test function  $\mathbf{v} = v_r \mathbf{e}_r + v_z \mathbf{e}_z$ , (ii) integrate by parts on  $\Omega$ , (iii) replace  $\sigma_{ij}$  by functions of  $u_i$  using (4) and (1c), and (iv) incorporate the boundary conditions of (7), letting  $\mathbf{v}$  take on homogeneous displacement boundary conditions on  $\Gamma_{\text{disp}}$ . The result is the equation

$$\int_{\Omega} \mathbf{E}(\underline{\epsilon}(\mathbf{u}) - \underline{\gamma}) : \underline{\epsilon}(\mathbf{v}) r \, dr dz - \int_{\Gamma_{\text{trac}}} \mathbf{g}_{\text{trac}} \cdot \mathbf{v} r \, ds = - \int_{\Omega} \mathbf{f} \cdot \mathbf{v} r \, dr dz. \quad (9)$$

Here the colon denotes the Frobenius inner product. To simplify notation, we let  $(\cdot, \cdot)_r$  and  $\langle \cdot, \cdot \rangle_r$  respectively denote the integrals over  $\Omega$  and  $\Gamma_{\text{trac}}$  of  $r$  multiplied by the appropriate (dot or Frobenius) inner product of the arguments. Then the above equation may be rewritten as

$$(\mathbf{E}\underline{\epsilon}(\mathbf{u}), \underline{\epsilon}(\mathbf{v}))_r = -(\mathbf{f}, \mathbf{v})_r + \langle \mathbf{g}_{\text{trac}}, \mathbf{v} \rangle_r + (\mathbf{E}\underline{\gamma}, \mathbf{v})_r. \quad (10)$$

The Lagrange FEM is derived by imposing the above equation on a space of piecewise polynomials. Given a triangulation of  $\Omega$ , denoted by  $\Omega_h$ , the Lagrange finite element space

255 of order  $p$ , denoted by  $V_h$  consists of all functions which are continuous on  $\Omega$  whose  
 256 restriction to each element  $K$  of  $\Omega_h$  is a polynomial of degree at most  $p$  in  $r$  and  $z$ . The  
 257 method is high-order, meaning that polynomials of high degree within each mesh ele-  
 258 ment approximate the solution. When degree  $p$  is used within an element of diameter  
 259  $h$ , the solution can be approximated on that element at rate  $O(h^{p+1})$ . As  $h$  decreases,  
 260 the solution becomes smoother, thus using higher  $p$  means that the numerical solution  
 261 is more rapidly convergent than a low-order method. In the FEM, the data  $\mathbf{f}$  and  $\mathbf{g}_{\text{trac}}$   
 262 are integrated while the data  $\mathbf{g}_{\text{disp}}$  is interpolated. Assuming the latter interpolation is  
 263 done, let

$$264 \quad \mathbf{V}_h^{\mathbf{g}_{\text{disp}}} = \{\mathbf{v} = v_r \mathbf{e}_r + v_z \mathbf{e}_z : v_r \in V_h, v_z \in V_h, \text{ and } \mathbf{v}|_{\Gamma_{\text{disp}}} = \mathbf{g}_{\text{disp}}\}.$$

265 Also let

$$266 \quad \mathbf{V}_h^0 = \{\mathbf{v} = v_r \mathbf{e}_r + v_z \mathbf{e}_z : v_r \in V_h, v_z \in V_h, \text{ and } \mathbf{v}|_{\Gamma_{\text{disp}}} = \mathbf{0}\}.$$

267 Then, the FEM computes  $\mathbf{u}_h \in \mathbf{V}_h^{\mathbf{g}_{\text{disp}}}$  satisfying

$$268 \quad (\mathbf{E}\underline{\underline{\boldsymbol{\varepsilon}}}(\mathbf{u}_h), \underline{\underline{\boldsymbol{\varepsilon}}}(\mathbf{v}))_r = -(\mathbf{f}, \mathbf{v})_r + (\mathbf{g}_{\text{trac}}, \mathbf{v})_r + (\mathbf{E}\boldsymbol{\gamma}, \mathbf{v})_r, \quad \text{for all } \mathbf{v} \in \mathbf{V}_h^0, \quad (11)$$

269 provided  $\mathbf{f}$ ,  $\mathbf{g}_{\text{disp}}$ ,  $\mathbf{g}_{\text{trac}}$ , and  $\boldsymbol{\gamma}$  are given. Equation (11) leads to a linear system of equa-  
 270 tions once a finite element basis of shape functions (which are basis functions determin-  
 271 ing one degree of freedom in the finite element system) is used.

### 272 3.2 Temporal Discretization

273 Our time-stepping method is inspired by that of Allison and Dunham (2018) where  
 274 viscous strains appear as a time-dependent source term on the equilibrium equation: As  
 275 can be seen from Equation (11), once  $\boldsymbol{\gamma}$  is known at any given time, it appears as a known  
 276 term and a displacement approximation can be computed by solving (11). However, to  
 277 compute  $\boldsymbol{\gamma}$ , we need to apply a time integrator to the aging law, Equation (1b).

278 To this end, for computational purposes only it is convenient to let  $\underline{\underline{\mathbf{C}}} = \mathbf{E}\underline{\underline{\boldsymbol{\gamma}}}$ , since  
 279 the use of  $\underline{\underline{\mathbf{C}}}$  allows us to skip the assembly and inversion of a mass matrix made of in-  
 280 homogeneous material coefficients. Since  $\mathbf{E}$  is time independent, simplifying  $\mathbf{E}\mathbf{A}\underline{\underline{\boldsymbol{\sigma}}} =$   
 281  $(\mu/\eta)\text{dev}(\underline{\underline{\boldsymbol{\sigma}}})$ , Equation (1b) implies

$$282 \quad \dot{\underline{\underline{\mathbf{C}}}} = \frac{\mu}{\eta} \text{dev } \underline{\underline{\boldsymbol{\sigma}}}. \quad (12)$$

283 Here  $\text{dev}(\underline{\underline{\boldsymbol{\sigma}}})$  denotes deviatoric tensor  $\underline{\underline{\boldsymbol{\sigma}}} - \text{tr}(\underline{\underline{\boldsymbol{\sigma}}})$ . Time integration of Equation (12) is  
 284 carried out using the first-order accurate forward Euler method (chosen for its simplic-  
 285 ity as we lay the computational groundwork; higher order methods will be incorporated  
 286 in future developments). At each time step, we solve the weak form of equilibrium equa-  
 287 tion (Equation (11)) and use the computed displacement to obtain  $\underline{\underline{\mathbf{C}}}$  at the next time

288 step. To illustrate time-stepping explicitly, assume all fields are known at time  $t^n$ . The  
 289 procedure to integrate to  $t^{n+1}$  over step size  $\Delta t = t^{n+1} - t^n$  is as follows:

290 1. Use  $\mathbf{u}_h^n$  to update  $\underline{\mathbf{C}}$  via forward Euler

$$291 \quad \underline{\mathbf{C}}^{n+1} = \underline{\mathbf{C}}^n + \Delta t \frac{\mu}{\eta} \operatorname{dev}(\mathbf{E}\underline{\boldsymbol{\varepsilon}}(\mathbf{u}_h^n) - \underline{\mathbf{C}}^n). \quad (13)$$

292 2. Compute data  $\mathbf{f}^{n+1}$ ,  $\mathbf{g}_{\text{disp}}^{n+1}$ ,  $\mathbf{g}_{\text{trac}}^{n+1}$  at time  $t^{n+1}$  and use them, together with the out-  
 293 put of the previous step, to solve the static equation: compute  $\mathbf{u}_h^{n+1} \in \mathbf{V}_h^{\mathbf{g}_{\text{disp}}^{n+1}}$   
 294 satisfying

$$295 \quad (\mathbf{E}\underline{\boldsymbol{\varepsilon}}(\mathbf{u}_h^{n+1}), \underline{\boldsymbol{\varepsilon}}(\mathbf{v}))_r = -(\mathbf{f}^{n+1}, \mathbf{v})_r + \langle \mathbf{g}_{\text{trac}}^{n+1}, \mathbf{v} \rangle_r + (\underline{\mathbf{C}}^{n+1}, \mathbf{v})_r \quad (14)$$

296 for all  $\mathbf{v} \in \mathbf{V}_h^0$ .

297 Verification of both spatial and temporal convergence of this computational method fol-  
 298 lows in section 3.4.

### 299 3.3 Model Specifics and Non-Dimensionalization

300 The majority of analysis in this work will examine how a spatial distribution of vis-  
 301 coelastic properties impacts deformation around magma reservoirs subject to cyclic load-  
 302 ing. We proceed by idealizing the boundary pressure as a sinusoid, which approximates  
 303 a canonical problem in viscoelasticity (Golden & Graham, 1988), and provides a frame-  
 304 work for studying arbitrary time dependent signals through superposition. We thus as-  
 305 sume a specific boundary partition where  $\Gamma_{\text{trac}}$  encompasses the reservoir wall, Earth's  
 306 free surface, and the computational boundary at depth ( $z = -L_z$ ).  $\Gamma_{\text{disp}}$  is the lateral  
 307 boundary  $r = L_r$ . We then set specific boundary data

$$308 \quad \mathbf{g}_{\text{disp}}(t) = 0, \quad (15)$$

309 so that displacements vanish at  $r = L_r$ . At Earth's free surface and at depth we take

$$310 \quad \mathbf{g}_{\text{trac}}(t) = 0. \quad (16)$$

311 At the reservoir wall we set

$$312 \quad -\mathbf{n} \cdot \mathbf{g}_{\text{trac}}(t) = P(t), \quad (17a)$$

$$313 \quad \mathbf{m} \cdot \mathbf{g}_{\text{trac}}(t) = 0, \quad (17b)$$

314 where

$$315 \quad P(t) = P_0 \sin(\omega t). \quad (18)$$

316 Equation 17a sets the normal component of the traction vector (the pressure) equal to  
 317 a sinusoidal time-varying condition with amplitude  $P_0$  and frequency  $\omega$ . In what follows

318 we will often refer to forcing period

$$319 \quad \tau = 2\pi/\omega \quad (19)$$

320 rather than frequency. Equation 17b imposes that the shear component of traction be  
321 equal to 0, where vector  $\mathbf{m} = \mathbf{n} \times \mathbf{e}_z$  is tangent to the reservoir wall.

322 Non-dimensionalization of the governing equations reveals important physical pa-  
323 rameters and re-scales the problem to help reduce round-off errors. We begin by han-  
324 dling the scaling of the spatial domain before addressing governing equations. Tildes in  
325 what follows indicate non-dimensional variables. Let  $r = a\tilde{r}$ ,  $z = a\tilde{z}$ ,  $\tilde{\mathcal{D}} = \{(\tilde{r}, \tilde{z}) \in$   
326  $\mathbb{R}^2 \mid 0 \leq \tilde{r} \leq \frac{L_r}{a}, -\frac{L_z}{a} \leq \tilde{z} \leq \frac{D+b}{a}\}$  and  $\tilde{\mathcal{B}} = \{(\tilde{r}, \tilde{z}) \in \mathbb{R}^2 \mid \tilde{r}^2 + \frac{a^2}{b^2}\tilde{z} \geq 1\}$ . Then our  
327 resulting scaled domain is given by

$$328 \quad \tilde{\Omega} = \tilde{\mathcal{D}} \cap \tilde{\mathcal{B}}, \quad (20)$$

329 with scaled boundaries  $\tilde{\Gamma}_{\text{disp}}$  still representing the (scaled) lateral boundary and  $\tilde{\Gamma}_{\text{trac}}$   
330 the (scaled) reservoir wall, Earth's free surface, and computational boundary at depth.  
331 We also scale displacements by  $a$ , namely  $a\tilde{\mathbf{u}} = \mathbf{u}$ , which effectively means that total  
332 strain  $\underline{\epsilon}$  is not scaled. We scale stress and time by the amplitude and frequency of the  
333 sinusoidal pressure,  $\mathbf{E}$  by characteristic shear modulus  $\mu$  and body force by its magni-  
334 tude  $F_0$  (for example magnitude of gravitational force), giving

$$335 \quad \underline{\sigma} = P_0\tilde{\sigma}, \quad (21)$$

$$336 \quad \mathbf{E} = \mu\tilde{\mathbf{E}}, \quad (22)$$

$$337 \quad \mathbf{f} = F_0\tilde{\mathbf{f}}, \quad (23)$$

$$338 \quad t\omega = \tilde{t}, \quad (24)$$

339 which implies a scaling of  $\underline{\mathbf{C}} = P_0\tilde{\underline{\mathbf{C}}}$ . The scaled form of the equilibrium equation (1a)  
340 is thus

$$341 \quad \text{div } \tilde{\sigma} = \frac{aF_0}{P_0}\tilde{\mathbf{f}}, \quad (25)$$

342 and Hooke's law Equation (1c) becomes

$$343 \quad \tilde{\sigma} = \frac{\mu}{P_0}\tilde{\mathbf{E}}(\underline{\epsilon} - \underline{\gamma}). \quad (26)$$

344 The two dimensionless parameters in Equations 25-26 physically represent the ratio of  
345 body force to reservoir boundary tractions, and a scaled reservoir pressure, respectively.

346 The modified aging law (Equation (12)) becomes

$$347 \quad \partial_{\tilde{t}}\tilde{\underline{\mathbf{C}}} = \frac{1}{De} \text{dev } \tilde{\sigma}, \quad (27)$$

348 where

$$349 \quad De = \frac{\eta\omega}{\mu} = \frac{2\pi\eta}{\tau\mu} \quad (28)$$

350 is the non-dimensional Deborah number, a ratio of elastic pressurization timescale  $\tau/2\pi$   
 351 to Maxwell viscous relaxation timescale  $\eta/\mu$ , where viscosity  $\eta$ , shear modulus  $\mu$  and pres-  
 352 surization time  $\tau$  are understood to be characteristic scales if spatially or time variable.  
 353  $De$  commonly appears as a control parameter in models for magma chamber mechan-  
 354 ics (Jellinek & DePaolo, 2003; Hickey et al., 2015), cycles of eruptions (Degruyter & Hu-  
 355 ber, 2014; Black & Manga, 2017), and the spatial structure of transcrustal magma sys-  
 356 tems (Karlstrom et al., 2017; Huber et al., 2019). It will play an important role in our  
 357 results.

358 Computationally, all problems considered in this work are solved in this non-dimensional  
 359 form. The specific non-dimensional boundary conditions we thus take are

$$360 \quad \tilde{\mathbf{u}} = 0 \quad \text{on } \tilde{\Gamma}_{\text{disp}}, \quad (29a)$$

$$361 \quad \tilde{\boldsymbol{\sigma}}\mathbf{n} = \tilde{\mathbf{g}}_{\text{trac}}(\tilde{t}) \quad \text{on } \tilde{\Gamma}_{\text{trac}}, \quad (29b)$$

362 and at the reservoir wall,

$$363 \quad -\mathbf{n} \cdot \tilde{\mathbf{g}}_{\text{disp}}(\tilde{t}) = \tilde{P}(\tilde{t}) \quad (30)$$

$$364 \quad \mathbf{m} \cdot \tilde{\mathbf{g}}_{\text{trac}}(\tilde{t}) = 0. \quad (31)$$

365 where  $\tilde{P}(\tilde{t}) = \sin(\tilde{t})$ . For all our applications we assume negligible body forces, so  $aF_0/P_0 \ll$   
 366 1.

### 367 3.4 Stability and Verification

368 Owing to the use of an explicit time-stepping scheme, it is necessary to establish  
 369 conditions for which the scheme outlined in the previous section is stable. As an initial  
 370 calculation, note that

$$371 \quad \mathbf{E}\mathbf{A}\boldsymbol{\sigma} = \frac{\mu}{\eta} \text{dev } \boldsymbol{\sigma}. \quad (32)$$

372 The deviatoric operator in Equation (32) can be expressed as a matrix-vector multipli-  
 373 cation, namely

$$374 \quad \mathbf{E}\mathbf{A}\boldsymbol{\sigma} = \frac{\mu}{\eta} \mathcal{D}\boldsymbol{\sigma}, \quad (33)$$

375 if second-order tensors are stacked into vectors (across rows and removing symmetries)

$$376 \quad \boldsymbol{\sigma} = [\sigma_{rr}, \sigma_{rz}, \sigma_{zz}, \sigma_{\theta\theta}]^T, \quad (34)$$

377 and matrix  $\mathcal{D}$  is given by

$$378 \quad \mathcal{D} = \begin{bmatrix} \frac{2}{3} & -\frac{1}{3} & -\frac{1}{3} & 0 \\ -\frac{1}{3} & \frac{2}{3} & -\frac{1}{3} & 0 \\ -\frac{1}{3} & -\frac{1}{3} & \frac{2}{3} & 0 \\ 0 & 0 & 0 & 1 \end{bmatrix}. \quad (35)$$

379 The non-dimensionalized explicit forward-Euler discretization of the aging law (Equa-  
 380 tion (27)) can therefore be expressed as

$$381 \quad \tilde{\mathbf{C}}^{n+1} = (\mathbf{I} - \Delta\tilde{t}De^{-1}\mathcal{D})\tilde{\mathbf{C}}^n + \Delta\tilde{t}De^{-1}\mathcal{D}\tilde{\mathbf{E}}\underline{\boldsymbol{\epsilon}}^n, \quad (36)$$

382 the stability of which is determined by the eigenvalues of the growth-factor matrix  $\mathbf{I}-$   
 383  $\Delta\tilde{t}De^{-1}\mathcal{D}$  and whether we can bound its spectral radius using an appropriate choice for  
 384  $\Delta\tilde{t}$ . Eigenvalues for the growth-factor matrix are

$$385 \quad \lambda_1 = 1, \quad (37a)$$

$$386 \quad \lambda_2 = 1 - \frac{2}{3}\Delta\tilde{t}De^{-1}, \quad (37b)$$

$$387 \quad \lambda_3 = 1 - \Delta\tilde{t}De^{-1}, \quad (37c)$$

388 where  $\lambda_3$  appears as a repeated eigenvalue. To bound their magnitudes by at most 1 de-  
 389 mands that  $\Delta\tilde{t}$  be smaller than  $2De$ . In addition, the time step must be sufficiently small  
 390 to resolve any time-varying boundary data. In this work this amounts to resolving the  
 391 sinusoidal boundary data at the reservoir wall. Since the corresponding (angular) Nyquist  
 392 frequency for  $\sin(\tilde{t})$  is 1, the largest time step that resolves this frequency is  $\delta\tilde{t} = \pi$ , and  
 393 should be (in practice) a small fraction of this. A sufficient, stable time step is then cho-  
 394 sen by

$$395 \quad \Delta\tilde{t} \leq \min\{2De, \delta\tilde{t}\}. \quad (38)$$

396 In practice we use more restrictive criteria, namely,

$$397 \quad \Delta\tilde{t} \leq \min\left\{\frac{De}{4}, \frac{\delta\tilde{t}}{2}\right\}. \quad (39)$$

398 Except for a few limiting cases, the temperature-dependent material parameters will cause  
 399  $\frac{De}{4}$  to be the agent that restricts time-step.

400 Our numerical method is verified for correctness via rigorous convergence tests in  
 401 both space and time via the method of manufactured solutions (MMS) (Roache, 1998),  
 402 with details provided in Appendix A. Code verification could also be done via compar-  
 403 isons against simple analytic models (Hickey & Gottsmann, 2014), or benefit from com-  
 404 munity benchmark efforts, which we further discuss in Appendix A.

### 405 **3.5 Temperature-Dependent Material Parameters**

406 We assume that viscosity of crustal rocks is described by a temperature-dependent  
 407 Arrhenius relation, an assumption common to many thermomechanical models of mag-  
 408 matic systems (e.g., Del Negro et al., 2009). This neglects grain-size and stress-dependent  
 409 effects (Bürgmann & Dresen, 2008), but parameterizes our assumption that tempera-  
 410 ture is the dominant factor controlling crustal rheology during crustal magma transport.

411 In general, temperature evolves in time in response to magmatism (e.g., Karakas et al.,  
 412 2017), but we assume a steady state geotherm here as our goal is simply to explore the  
 413 role of realistic spatial structure of material parameters.

414 Accordingly, we solve the stationary heat equation

$$415 \quad \nabla^2 T = 0 \quad \text{in } \check{\Omega}, \quad (40)$$

416 where  $T(r, z)$  is the temperature field, which we assume to be axisymmetric. At the top,  
 417 bottom and lateral parts of the boundary, we enforce a steady-state geothermal profile  
 418 given by

$$419 \quad T(z) = T_s - \alpha(z - (D + b)), \quad (41)$$

420 where  $T_s$  is the surface temperature constant and  $\alpha$  is a parameter specifying the tem-  
 421 perature gradient. At the chamber wall we set  $T = T_c$ , a constant temperature. We  
 422 use a finite element space of order  $p$  to solve the heat equation. Here,  $p$  is the same or-  
 423 der as is used in the finite element solution of the equilibrium equation. The formula-  
 424 tion uses radial weighting to reduce the problem to the two-dimensional domain  $\Omega$  and  
 425 as usual—see e.g., Gopalakrishnan and Pasciak (2006)—set zero temperature flux  $\nabla T =$   
 426  $0$  at  $\Gamma_0$ , the  $r = 0$  boundary, to maintain our consideration of a one-sided problem. The  
 427 solution of this BVP for the heat equation informs the temperature field throughout the  
 428 domain, from which the viscosity is deduced according to the Arrhenius formula

$$429 \quad \eta = A_D \exp\left(\frac{E_a}{RT}\right) \quad (42)$$

430 where  $A_D$  is the Dorn parameter,  $E_a$  is the activation energy, and  $R$  is the Boltzmann  
 431 constant. For numerical computation, we prefer to use the equivalent formula

$$432 \quad \eta = \eta_0 \exp\left(\frac{E_a}{R} \left[\frac{1}{T} - \frac{1}{T_s}\right]\right), \quad (43)$$

433 where  $\eta_0 = A_D \exp\left(\frac{E_a}{RT_s}\right)$ , to avoid numerical issues associated with very large viscosi-  
 434 ties predicted by low temperatures in the near surface. In Equation 43 we use absolute  
 435 temperature, so both  $T$  and  $T_s$  should be converted from degrees Celsius to Kelvin.

436 Because numerically stable time steps depend on Deborah number (i.e. Equation  
 437 38) in our approach, the exponential dependence of viscosity leads to prohibitively small  
 438 time steps at high temperatures. This limits the degree to which we can exactly explore  
 439 high magma temperatures without artificially thresholding model temperature.

440 Elastic parameters are also considered to be temperature dependent. Bakker et al.  
 441 (2016) provide smooth and continuous forms for temperature-dependent Young's mod-



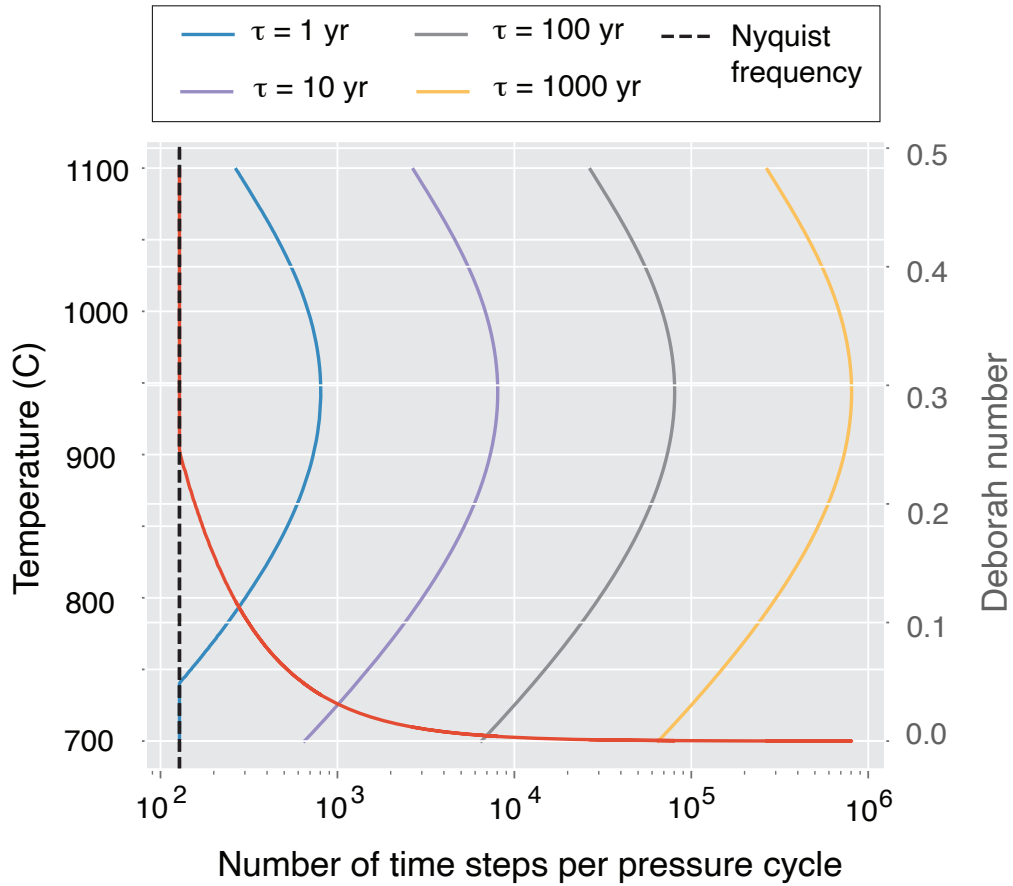


**Figure 2.** Number of timesteps required to simulate pressure forcing of various periods. Number of timesteps decreases with increasing Deborah number (red curve), until the Nyquist limit is reached (dashed curve). Number of timesteps per period is a non-monotonic function of temperature (other colored curves) because both elastic moduli and viscosity are temperature dependent.

442 ulus  $E(T)$  and Poisson's ratio  $\nu(T)$  as

$$443 \quad E(T) = c_1 \left[ 1 - \operatorname{erf} \left( \frac{T - \bar{T}}{s} \right) \right] + c_2 T + c_3, \quad (44)$$

$$444 \quad \nu(T) = \left[ 1 - \frac{E}{E_{\max}} \right] \cdot [\nu_{\max} - \nu_{\min}] + \nu_{\min} \quad (45)$$

445 where  $\nu_{\min} = 0.25, \nu_{\max} = 0.49$  define the range of possible Poisson's ratios and  $E_{\max}$   
 446 is the max value Young's modulus achieves for a given temperature profile.  $\bar{T}$  is a tem-  
 447 perature threshold for which Young's modulus decreases by an order of magnitude and  
 448  $c_1, c_2, c_3, s$  are empirical parameters. To convert  $E$  and  $\nu$  to  $\lambda, \mu$  (the proper elastic mod-  
 449 uli for our framework), we use  $\lambda = \frac{E\nu}{(1+\nu)(1-2\nu)}, \mu = \frac{E}{2(1+\nu)}$ . Figure 3 demonstrates  
 450 the spatial pattern exhibited by the material parameters for a temperature profile char-  
 451 acterized by 800°C reservoir temperature, 0°C surface temperature and a geothermal gra-  
 452 dient of 20°C/km.

#### 453 **4 Analysis of time dependent viscoelastic deformation**

454 We now develop tools to analyze the time evolution of viscoelastic deformation pre-  
 455 dicted from our numerical calculations. Towards our goal of examining how a realistic  
 456 distribution of viscoelastic properties impacts deformation around magma reservoirs sub-  
 457 ject to cyclic loading, we begin with a 1D analysis of the Maxwell model to illustrate in-  
 458 herent properties of the system which may be generalized in the 2D problem. This anal-  
 459 ysis is easily generalizable to other viscoelastic models, and leads to concrete implica-  
 460 tions for inferring viscoelastic behavior in magmatic systems from ground deformation.

##### 461 **4.1 Insights from the 1D Maxwell Model**

462 Given the spatial domain  $x \in [0, L]$ , the 1D strain-displacement relation is given  
 463 by

$$464 \quad \varepsilon = u_x \quad (46)$$

465 and the 1D governing equations (equilibrium, viscous strain evolution and Hooke's law,  
 466 respectively) are

$$467 \quad \frac{\partial \sigma}{\partial x} = 0, \quad (47a)$$

$$468 \quad \dot{\gamma} = \frac{1}{\eta} \sigma, \quad (47b)$$

$$469 \quad \sigma = \mu(\varepsilon - \gamma), \quad (47c)$$

470 where  $\sigma, \varepsilon, \gamma,$  and  $u$  are, respectively, the 1D stress, total strain, viscous strain, and dis-  
 471 placement. Boundary conditions are chosen to reflect the conditions for the 2D problem.  
 472 The origin experiences the sinusoidal pressure condition (representing the reservoir) and

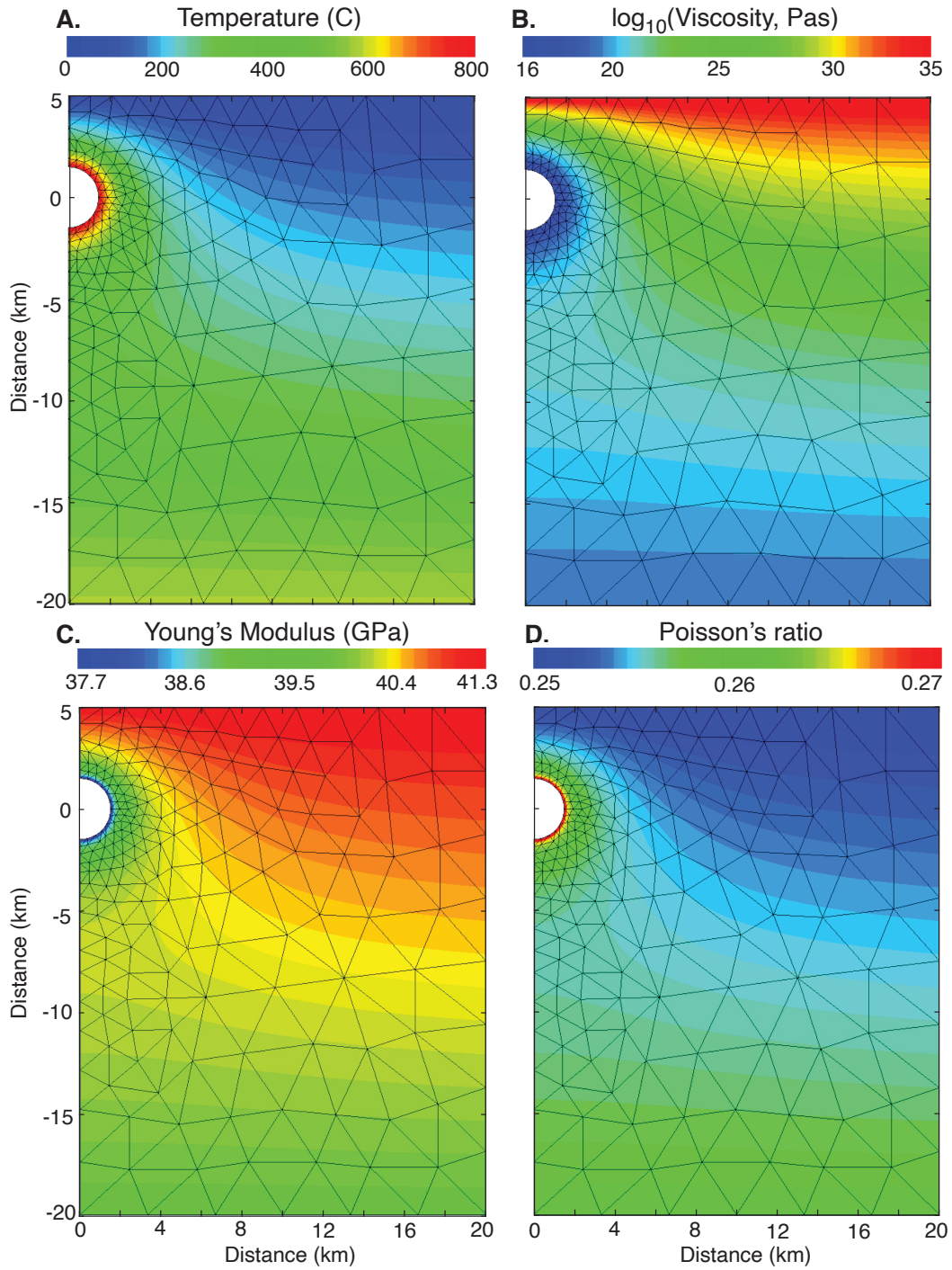


**Figure 3.** Material parameters used in our reference variable coefficients parameter study, with finite element mesh overlaid. **A.** Temperature, obtained by solving Equation 40 with  $T_c = 800^\circ\text{C}$ , surface temperature  $T_s = 0^\circ\text{C}$ , and geothermal gradient  $\alpha = 20^\circ\text{C}/\text{km}$ . **B.** Viscosity from Equation 43. **C.** Young's Modulus from Equation 44. **D.** Poisson's ratio from Equation 45.

473 displacements vanish at the far boundary, namely

$$474 \quad \sigma(x = 0, t) = \sin(\omega t), \quad (48a)$$

$$475 \quad u(x = L, t) = 0. \quad (48b)$$

476 We consider  $t > 0$ ; the aging law Equation 47b thus requires an initial viscous strain  
477 to be specified, which we express in general terms

$$478 \quad \gamma(x, t = 0) = \gamma_0(x), \quad (49)$$

479 where  $\gamma_0$  as a given function. The Maxwell model thus gives rise to an initial-boundary  
480 value problem defined by Equations 46-49.

481 We are interested in the response between stress and strain at the reservoir bound-  
482 ary, with the expectation that viscous relaxation will lead to a phase difference. To do  
483 this analysis it is useful to work with Hooke's law in rate form, namely,

$$484 \quad \dot{\epsilon} = \frac{1}{\mu} \dot{\sigma} + \frac{1}{\eta} \sigma. \quad (50)$$

485 Following Golden and Graham (1988), application of the Fourier transform to Equation  
486 50 yields the constitutive law in frequency space

$$487 \quad \hat{\sigma}(\omega) = \hat{\mu}(\omega) \hat{\epsilon}(\omega), \quad (51)$$

488 which gives the usual relationship where stress is expressed as a function of strain through  
489 a complex shear modulus  $\hat{\mu}$  defined by

$$490 \quad \hat{\mu}(\omega) = \left( \frac{1}{\mu} - i \frac{1}{\eta\omega} \right)^{-1}. \quad (52)$$

491 The decomposition  $\hat{\mu}(\omega) = \hat{\mu}_1(\omega) + i\hat{\mu}_2(\omega)$  into storage and loss moduli allows us to  
492 express  $\hat{\mu}$  as

$$493 \quad \hat{\mu}(\omega) = |\hat{\mu}(\omega)| e^{-i\delta} \quad (53)$$

494 where  $\delta = -\tan^{-1}\left(\frac{\hat{\mu}_2}{\hat{\mu}_1}\right)$ .

495 In our applications, however, we are interested in the strain response to an applied  
496 (sinusoidal) stress, thus we must consider the constitutive relation Equation 51 in the  
497 form

$$498 \quad \hat{\epsilon}(\omega) = \hat{d}(\omega) \hat{\sigma}(\omega), \quad (54)$$

499 where  $\hat{d}(\omega) = 1/\hat{\mu}(\omega)$  is the complex creep modulus given by

$$500 \quad \hat{d}(\omega) = \frac{1}{\mu} - i \frac{1}{\eta\omega}, \quad (55)$$

501 which can be decomposed into  $\hat{d}(\omega) = \hat{d}_1(\omega) + i\hat{d}_2(\omega)$  as before, and gives rise to the  
502 similar form

$$503 \quad \hat{d}(\omega) = |\hat{d}(\omega)| e^{-i\beta}, \quad (56)$$

504 for  $\beta = -\tan^{-1}\left(\frac{\hat{d}_2(\omega)}{\hat{d}_1(\omega)}\right)$ . Applying the inverse Fourier transform to Equation 54 and  
 505 using 48a yields

$$\begin{aligned}
 506 \quad \varepsilon(t) &= [d * \sigma](t), \\
 507 &= \hat{d}_1(\omega) \sin \omega t + \hat{d}_2(\omega) \cos \omega t, \\
 508 &= \sin(\omega t - \beta), \tag{57}
 \end{aligned}$$

509 which gives strain as an explicit function of stress, delayed by phase lag  $\beta$ . Since  $\hat{d}$  is chosen  
 510 as the multiplicative inverse of  $\hat{\mu}$  note that

$$511 \quad |\hat{d}(\omega)| = \frac{1}{|\hat{\mu}(\omega)|}, \tag{58a}$$

$$512 \quad \beta = -\delta, \tag{58b}$$

513 therefore the phase lag that strain experiences in response to an applied stress will be  
 514 equal and opposite when reversing roles and considering stress in response to an applied  
 515 strain. Note that we have used the sign convention for the phase lag such that positive  
 516 values of  $\beta$  correspond to strain lagging behind stress.

517 To summarize, the strain response to a sinusoidal stress is also sinusoidal with a  
 518 phase lag  $\beta$ , which can be simplified in terms of the Deborah number  $De$  by substituting  
 519 in the real and imaginary parts of  $\hat{d}(\omega)$ , resulting in

$$520 \quad \beta = \tan^{-1}\left(\frac{1}{De}\right). \tag{59}$$

521 This analytic result provides insight into the physics of the viscoelastic model, as two  
 522 limiting cases of the Deborah number (namely  $De \rightarrow \infty$  and  $De \rightarrow 0$ ) yield phase lags  
 523 of 0 and  $\pi/2$  (respectively) corresponding to the elastic and viscous limits (respectively).  
 524 In addition, these analytic results can be generalized to higher dimensions which we do  
 525 in the next section, providing useful code verification metrics as well as providing insight  
 526 into the frequency response of more physically realistic modeling scenarios.

## 527 **4.2 Transfer Function and Analytic Signals**

528 The phase lag analysis for the 1D problem of the previous section can be gener-  
 529 alized using the theory of Linear Time-Invariant (LTI) systems such as the viscoelastic  
 530 problem we consider here. For general LTI systems, one can characterize some output  
 531 signal  $y(t)$  as the linear transformation of a system input  $x(t)$ , where we consider one-  
 532 sided signals (i.e. they are 0 for  $t < 0$ ) (Schetzen, 2003). The response  $y$  can be deter-  
 533 mined as a convolution of the input  $x$  with the system impulse response  $h$ , namely

$$\begin{aligned}
 534 \quad y(t) &= (x * h)(t) \\
 535 &= \int_0^t x(t')h(t-t') dt'. \tag{60}
 \end{aligned}$$

536 The transfer function connecting the output signal  $y(t)$  given the input signal  $x(t)$  we  
 537 denote  $H\{y(t)|x(t)\}(i\omega)$ , however we drop the argument within curly braces or func-  
 538 tional dependence within parenthesis when these is implied via context. The transfer func-  
 539 tion is defined as

$$\begin{aligned}
 540 \quad H(i\omega) &= \mathcal{L}\{h\}(i\omega) \\
 541 \quad &= \frac{\mathcal{L}\{y\}}{\mathcal{L}\{x\}}(i\omega), \tag{61}
 \end{aligned}$$

542 where  $\mathcal{L}$  denotes the Laplace transform (a function of the complex variable  $s$ ) and we  
 543 have evaluated at  $s = i\omega$ . The transfer function thus provides the amplitude of the sys-  
 544 tem output as a function of frequency of the input signal. As an example, Equation 54  
 545 illustrates how  $\hat{d} = H\{\varepsilon(t)|\sigma(t)\}$ , i.e the transfer function when stress is the input sig-  
 546 nal and strain is the output.

547 If we consider specific input and output signals  $x(t) = A_{in} \sin(\omega t)$  and  $y(t) = A_{out} \sin(\omega t -$   
 548  $\phi)$ , then we can use the Laplace transform to calculate the transfer function, namely,

$$\begin{aligned}
 549 \quad H(i\omega) &= \frac{A_{out}}{A_{in}} \frac{(-s \sin(\phi) + \omega \cos(\phi))/(s^2 + \omega^2)}{\omega/(s^2 + \omega^2)} \Bigg|_{s=i\omega} \\
 550 \quad &= \frac{A_{out}}{A_{in}} e^{-i\phi}, \tag{62}
 \end{aligned}$$

551 i.e. a constant, independent of  $\omega$ . Performing an inverse Laplace transform indicates that  
 552 the corresponding system impulse response is a delta function, namely,  $h(t) = (A_{out}/A_{in})\delta(t -$   
 553  $\phi/\omega)$ .

554 Equation 62 illustrates the important point that evaluation at  $s = i\omega$  must take  
 555 place after the ratio is computed, so that the poles in the Laplace transforms of the si-  
 556 nusoids  $x$  and  $y$  are removed. In numerical studies making use of the discrete Fourier  
 557 transform, this evaluation cannot be done after the ratio is computed, which can lead  
 558 to division by zero. An alternative means for defining the transfer function therefore is  
 559 via the concept of analytic signals, which have straight-forward numerical approxima-  
 560 tions and avoid potential division by zero.

561 Analytic signals are defined in the following manner. Consider the real valued sig-  
 562 nal  $z(t)$  and denote its Fourier transform by  $\hat{z}(\xi)$ . Define the function

$$563 \quad \hat{z}_a(\xi) = 2\mathcal{H}(\xi) \hat{z}(\xi) \tag{63}$$

564 (where  $\mathcal{H}$  is the Heaviside step function), which contains only the non-negative frequency  
 565 components of  $\hat{z}(\xi)$ . The analytic signal corresponding to  $z$ , denoted  $z_a(t)$ , is a complex-  
 566 valued function obtained by transforming  $\hat{z}_a$  back to the time domain using the inverse  
 567 Fourier transform, yielding

$$568 \quad z_a(t) = z(t) + i\mathbb{H}\{z\}(t), \tag{64}$$

569 where  $\mathbb{H}$  is the Hilbert transform. Properties of Hilbert transforms mean that for input  
570 signal  $x(t)$  and response signal  $y(t)$  of an LTI system, we have that

$$571 \quad y_a(t) = (h * x_a)(t). \quad (65)$$

572 Considering the analytic signals  $x_a(t) = -iA_{\text{in}}e^{i\omega t}$  and  $y_a(t) = -iA_{\text{out}}e^{i(\omega t - \phi)}$  asso-  
573 ciated with the input and output signals under consideration, plugging these into (65)  
574 yields

$$575 \quad A_{\text{out}}e^{i(\omega t - \phi)} = A_{\text{in}}e^{i\omega t}H(i\omega). \quad (66)$$

576 Equation (66) illustrates the fact that for an input signals of form  $e^{i\omega t}$  (called a char-  
577 acteristic function), the response signal is given by  $e^{i\omega t}H(i\omega)$ , indicating that the out-  
578 put signal is simply a scaling of the input by  $H(i\omega)$ .

579 We can solve (66) for the transfer function, namely,

$$580 \quad H(i\omega) = \frac{A_{\text{out}}}{A_{\text{in}}}e^{-i\phi}, \quad (67)$$

581 previously obtained using Laplace transforms. The amplitude  $|H| = \left|\frac{A_{\text{out}}}{A_{\text{in}}}\right|$  is often re-  
582 ferred to as the gain because it describes how the frequency content in the output sig-  
583 nal is amplified in response to the input. And finally,  $\phi = -\arg(H)$  is the phase lag,  
584 which agrees with that of the 1D Maxwell model considered in the previous section.

585 As a corollary, if the transfer function is known, we may directly relate the input  
586 and output signals. For example, let  $x(t) = A \sin(\omega t - \psi)$ , with phase  $\psi$ , be an input  
587 signal and let  $H(i\omega) = |H(i\omega)|e^{-i\phi}$  be the transfer function. The analytic input sig-  
588 nal is then  $x_a(t) = -iAe^{i(\omega t - \psi)}$  and (65) implies that the the analytic output signal  
589 is  $y_a(t) = H(i\omega)x_a(t)$ . The desired output signal  $y(t)$  can be recovered by taking the  
590 real part of its analytic signal, namely

$$591 \quad y(t) = |H(i\omega)|A \sin(\omega t - \psi - \phi). \quad (68)$$

592 In other words, a sinusoidal input function implies a sinusoidal output function, mod-  
593 ulated by a phase lag  $\phi$  and amplitude gain  $|H|$ .

594 If  $\{A_k\}_{k=1}^n$ ,  $\{\omega_k\}_{k=1}^n$ ,  $\{\psi_k\}_{k=1}^n$  are sequences of amplitudes, frequencies, and phases,  
595 respectively, then a composite input signal can be expressed

$$596 \quad x(t) = \sum_{k=1}^n A_k \sin(\omega_k t - \psi_k). \quad (69)$$

597 Note that each component is associated with a period  $\tau_k = 2\pi/\omega_k$ . By superposition,  
598 if  $\{H(i\omega_k)\}_{k=1}^n$  are (known) associated transfer functions with phase lags  $\{\phi_k\}_{k=1}^n$ , then  
599 the corresponding output signal is given by

$$600 \quad y(t) = \sum_{k=1}^n |H(i\omega_k)|A_k \sin(\omega_k t - \psi_k - \phi_k). \quad (70)$$

601 In discussion section 6, we illustrate this result for a specific composite input function  
 602 defining magma reservoir pressure through time and numerically calculated transfer func-  
 603 tion for resulting surface displacements.

604 In the sections that follow, we explore numerically how the transfer function links  
 605 reservoir pressure to surface displacements and strains. Following the notation for the  
 606 transfer function, we let  $\phi\{y(t) | x(t)\}$  denote the phase lag between the output signal  
 607  $y(t)$  given the input signal  $x(t)$ , but drop the argument in curly braces when it is implied  
 608 via context.

### 609 4.3 Numerical Calculations of the Transfer Function

610 The analytic signal corresponding to a real, discrete time-series is implemented in  
 611 the Python SciPy library via the `scipy.signal.hilbert()` function. The transfer func-  
 612 tion connecting an input signal  $x(t)$  to output signal  $y(t)$  is computed via the ratio of  
 613 corresponding analytic signals, from which we can compute phase and amplitude. All  
 614 scripts are available in the code repository. In practice, there exists an initial spin-up pe-  
 615 riod ( $\sim 4$  cycles) before solutions settle into a sinusoidal response and it is necessary to  
 616 compute the transfer function once out of this phase.

617 In addition to the spin-up phase, the output signal can be shifted to oscillate around  
 618 a non-zero value, which can complicate the calculation of the phase lag using our numer-  
 619 ical techniques. The 1D analysis of the previous section illustrates why this occurs. Spec-  
 620 ifying the initial condition Equation 49 impacts the evolution of the displacement and  
 621 stress fields in the following way: suppose  $\gamma_0(x) = 0$  for each  $x \in [0, L]$ . We can sim-  
 622 plify the boundary condition Equation 48 by taking  $P_0 = \omega = 1$ . The sinusoidal pres-  
 623 sure imposed at the left boundary along with Equation 47a imply a uniform stress field

$$624 \quad \sigma(t, x) = \sin t. \quad (71)$$

625 Integrating Equation 47b yields the viscous strain

$$626 \quad \gamma(t) = -\frac{1}{\eta} \cos t + \frac{1}{\eta}, \quad (72)$$

627 and solving Equation 47c for total strain gives the solution

$$628 \quad \varepsilon(t) = \frac{1}{\mu} \sin t - \frac{1}{\eta} \cos t + \frac{1}{\eta}, \quad (73)$$

629 which illustrates how the strain response is sinusoidal with a shift of  $1/\eta$ . Although strain  
 630 starts initially at 0, it fluctuates around the non-zero value  $1/\eta$ , corresponding to a vol-  
 631 ume change (length change in 1D). To avoid this situation, one could specify a differ-  
 632 ent initial viscous strain, i.e.  $\gamma_0(x) = -1/\eta$  which would yield a strain response fluc-  
 633 tuating around zero. In the 2D problems considered in this work, it is difficult to know



634 a priori the initial viscous strain that would preclude a volume change. Thus to com-  
 635 pare the phase-lag response, fields that do not fluctuate around zero must first be shifted  
 636 to do so. The spin-up phase contributes an exponentially decaying component in the out-  
 637 put signal, therefore we calculate approximate phase and amplitude after 4 pressuriza-  
 638 tion cycles.

639 The sinusoidal pressure forcing we impose at the reservoir wall given by Equation  
 640 17a is considered the input signal  $P(t)$  for all of our studies. To verify correctness of our  
 641 numerical methods, we first consider as the output signal the normal component of strain  
 642 at a single spatial point on the wall, namely  $\varepsilon_{rr}(r = a, z = 0, t)$ . Because at the reser-  
 643 voir wall the stress-strain relation effectively reduces to a 1D problem at a point, our nu-  
 644 meric calculations are verified by comparing our numerical calculations of transfer func-  
 645 tion amplitude and phase lag against the theoretical stress-strain relationship for a Maxwell  
 646 material for different forcing periods  $\tau$  (see Equation 19), as evidenced in Figure 4. In  
 647 addition we compute the phase lag observed in the vertical component of displacement  
 648 at Earth’s surface  $u_z(r = 0, z = D + b, t)$  as well as the transfer function amplitude  
 649 (gain).

## 650 5 Computational Results

651 Viscoelastic behavior of magma reservoirs is often characterized in terms of defor-  
 652 mation of a flat free surface induced by pressurization of a spheroidal reservoir (e.g., Segall,  
 653 2016; Head et al., 2019; Townsend, 2022). Even in this relatively simple case, the prob-  
 654 lem is complex because a large number of control parameters matter and trade off in non-  
 655 unique ways to generate surface deformation patterns. An additional challenge is that  
 656 the problem is generally not amenable to analytic analysis such as has been conducted  
 657 in simplified limits (Dragoni & Magnanensi, 1989; Karlstrom et al., 2010; Bonafede et  
 658 al., 1986).

659 Having established our computational framework, we will now focus on a specific  
 660 and relatively unexplored part of this problem here, the frequency dependence of sur-  
 661 face deformation. All fixed parameters used in this study are listed in Table 1, unless  
 662 otherwise noted. In the constant coefficient case studied in Figure 4 (a spherical reser-  
 663 voir in a uniform viscoelastic halfspace), sinusoidal forcing at the reservoir wall results  
 664 in surface deformation patterns that are simply parameterized in terms of the Deborah  
 665 number (Equation 59).  $De \approx 10$  signifies the onset of viscous response in host rocks,  
 666 while for  $De < 1$  the host rock response is dominantly viscous in the sense that phase  
 667 lag  $\phi$  between surface deformation is more than halfway to the viscous limit.

**Table 1.** Parameters used in Applications (unless otherwise noted).

Symbol	Explanation	Value
$a$	Ellipse semi-major axis	1500 m
$b$	Ellipse semi-minor axis	1500 m
$D$	Reservoir depth beneath Earth's surface	3500 m
$L_r$	Domain length in radial direction	20000 m
$L_z$	Domain length in vertical direction	20000 m
$P_0$	Reservoir pressure amplitude	10 MPa
$A_D$	Dorn parameter	$10^9$ Pa s
$A$	Material-dependent constant for viscosity	$4.25 \times 10^7$ Pa s
$E_a$	Activation energy	141 kJ/(mol)
$R$	Boltzmann's molar gas constant	8.314 J/(mol K)
$T_c$	Reservoir temperature	800°C
$T_s$	Surface temperature	0°C
$\alpha$	Geothermal gradient	20°C/km
$\nu_{\min}$	Min Poisson's ratio	0.25
$\nu_{\max}$	Max Poisson's ratio	0.49
$E_{\max}$	Max Young's modulus	$4.0 \times 10^{10}$ Pa
$c_1$	Parameter in model for E	$1.8 \times 10^{10}$ Pa
$c_2$	Parameter in model for E	$-3.5 \times 10^6$ Pa/°C
$c_3$	Parameter in model for E	$4.3 \times 10^9$ Pa
$s$	Parameter in model for E	120 °C
$\bar{T}$	Temperature threshold	924°C

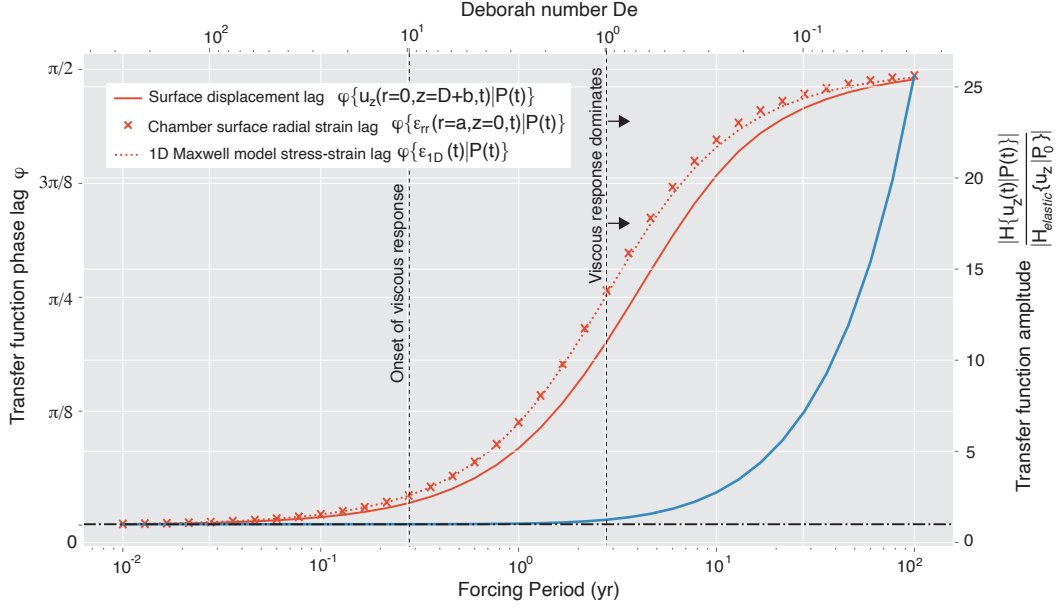


**Figure 4.** Phase lag  $\phi$  of the transfer function between reservoir pressure and radial strain at the reservoir wall ( $\phi\{\epsilon_{rr}(r = a, z = 0, t|P(t))\}$ , red dashed curve) and vertical displacement at the surface overlying the reservoir ( $\phi\{u_z(r = 0, z = D + b, t|P(t))\}$ , solid red curve). Crosses come from the 1D analytic prediction (Equation 59). Right axis and blue curve plot the amplitude of the transfer function  $|H\{u_z(r = 0, z = D + b, t|P(t))\}|$  normalized by the transfer function amplitude in a purely elastic limit (which uses the same averaged elastic coefficients but with  $\eta = 1 \times 10^{34}$  making viscous effects negligible). Upper x axis is the Deborah number, lower x-axis dimensionalizes into period of sinusoidal pressure forcing using  $\eta = 2.20 \times 10^{17}$  Pas,  $\lambda = 16.7$  GPa and  $\mu = 16.0$  GPa. Vertical dashed lines correspond to threshold Deborah numbers associated with onset of viscous response in host rocks.

668 We construct constant coefficient models by choosing constant values of elastic pa-  
 669 rameters  $\mu$  and  $\lambda$  through spatially averaging the non-constant coefficient calculations  
 670 (Figure 4, bottom axis). For viscosity we suppose that a forcing period of 1 year yields  
 671 a surface phase lag of 0.3 rad. From this phase lag we compute the associated Deborah  
 672 number and solve Equation 28 for viscosity. The resulting constant material parameters  
 673 are:  $\mu = 16.0$  GPa,  $\lambda = 16.7$  GPa,  $\eta = 2.20 \times 10^{17}$  Pa.s. We can then associate a Deb-  
 674 orah number  $De$  with a forcing period  $\tau$  via Equation 28 and examine the transition to  
 675 a viscous response as a function of forcing period. In this example  $\tau = 1$  yr corresponds  
 676 to maximum surface displacement that lags behind maximum chamber pressure by  $\sim 16$   
 677 days at similar amplitude to the elastic limit, while  $\tau = 10$  yr corresponds to a phase  
 678 lag of  $\sim 1.9$  years with  $\sim 3\times$  amplitude to the elastic limit.

679 However, uniform viscosity is a poor approximation to crustal rheology in magmatic  
 680 regions. To understand what changes with more realistic temperature-dependent viscos-  
 681 ity and elastic constants, we also study how pressure forcing period affects ground de-  
 682 formation in the variable coefficient problem outlined in Section 3.3.

683 Figure 5 left axes show time series of maximum vertical surface displacement and  
 684 radial strain at the reservoir wall (plotted versus dimensionless time) for several repre-  
 685 sentative forcing periods  $\tau$  associated with forcing by cyclic pressurization of the cham-  
 686 ber (right axes). All quantities are normalized to facilitate comparison of phase lag as  
 687 a function of forcing period, with amplitudes given in the legend. We see that phase lag  
 688 differs in magnitude between surface and chamber wall.

689 Figure 6 plots the spatial variation in vertical and horizontal components of sur-  
 690 face displacements  $u_z, u_r$  as well as the scalar von Mises stress  $\sigma_v = \sqrt{3J_2}$  with  $J_2$  the  
 691 second deviatoric stress invariant for four positions in the pressure cycle ( $\omega = 0, \pi/2, \pi, 3\pi/2$   
 692 radians) and three forcing periods. Black and white contours represent level curves of  
 693 the spatially dependent Deborah number.

694 Finally, Figure 7 shows the transfer function phase  $\phi\{u_z(r = 0, z = D+b, t) | P(t)\}$   
 695 and normalized amplitude  $|H\{u_z(r = 0, z = D + b, t) | P(t)\}|/|H_{elastic}\{u_z(r = 0, z =$   
 696  $D + b) | P_0\}|$  for a sweep through pressure forcing period  $\tau$ . The elastic normalization  
 697  $H_{elastic}$  is computed for each temperature separately, due to temperature dependence  
 698 of elastic parameters  $E$  and  $\nu$  (non-constant coefficient corrections to the known spher-  
 699 ical cavity in half space elastic solution (Zhong et al., 2019)). Transfer function results  
 700 are computed for three choices of reservoir temperature  $T_c = 800, 900, 1000^\circ\text{C}$  in Fig-  
 701 ure 7. The simulations are carried out at 37 logarithmically-spaced forcing periods be-  
 702 tween 0.01yr and 100yr. For each forcing period and reservoir temperature, we compute

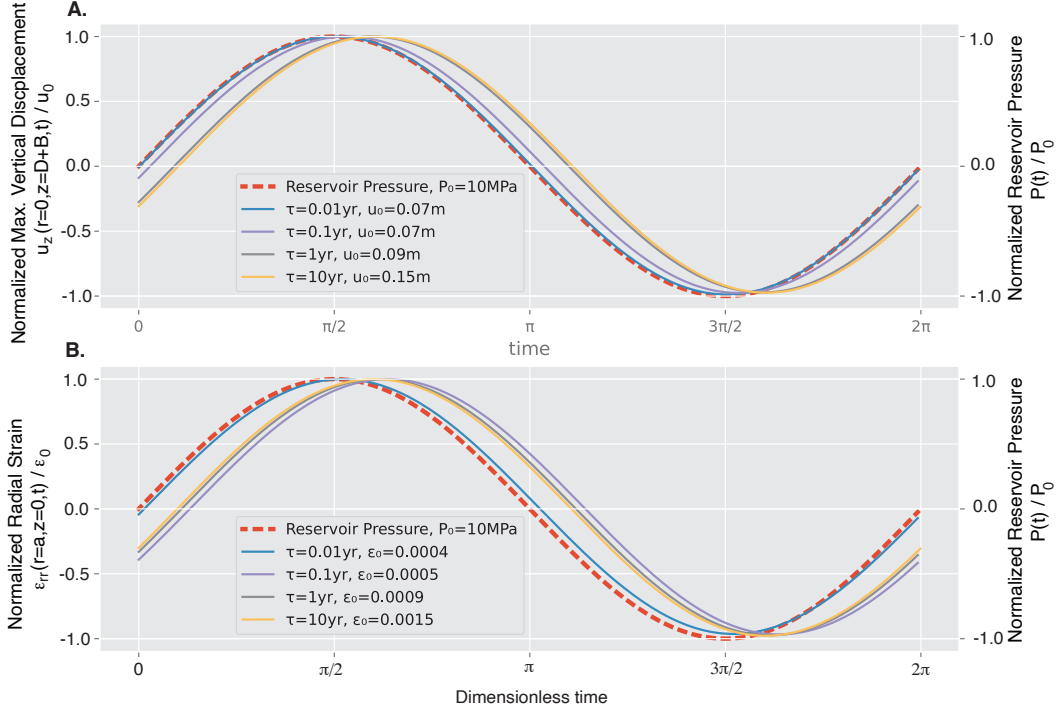


**Figure 5.** Temporal evolution (time non-dimensionalized by  $\tau$ ) associated with non-constant coefficient simulations at select forcing periods. Colored curves correspond to different forcing periods and normalization amplitudes  $u_0, \epsilon_0$ , dashed curves show pressure normalized by  $P_0$ . **A.** Normalized maximum vertical surface displacement. In dimensional time, peak vertical surface displacement for  $\tau = 0.01, 0.1, 1, 10$  years occurs 10.0 min, 12.7 hr, 17.6 days, and 6.3 months after peak reservoir pressure, respectively, associated with phase lags  $\phi\{u_z(r = 0, z = D + b, t|P(t))\} = 0.012, 0.091, 0.303$  and  $0.331$  radians. **B.** Normalized radial strain at the cavity wall, illustrating that phase offset of deformation from pressure forcing varies spatially through the domain.

703 the transfer function phase and amplitude over 10 complete pressurization cycles. Be-  
 704 cause of computational burden associated with the highest reservoir temperature of  $1000^\circ\text{C}$   
 705 (Figure 2) that lead to very small Deborah numbers, we set a maximal effective temper-  
 706 ature of  $900^\circ\text{C}$  for computing material parameters in this case. We also perform an ad-  
 707 ditional mesh refinement in space to mitigate poor resolution at longer forcing periods  
 708 for the  $1000^\circ\text{C}$  reservoir.

709 In contrast to the constant coefficient case, Figures 5-7 demonstrate that temper-  
 710 ature dependent material parameters strongly impact the frequency dependence of sys-

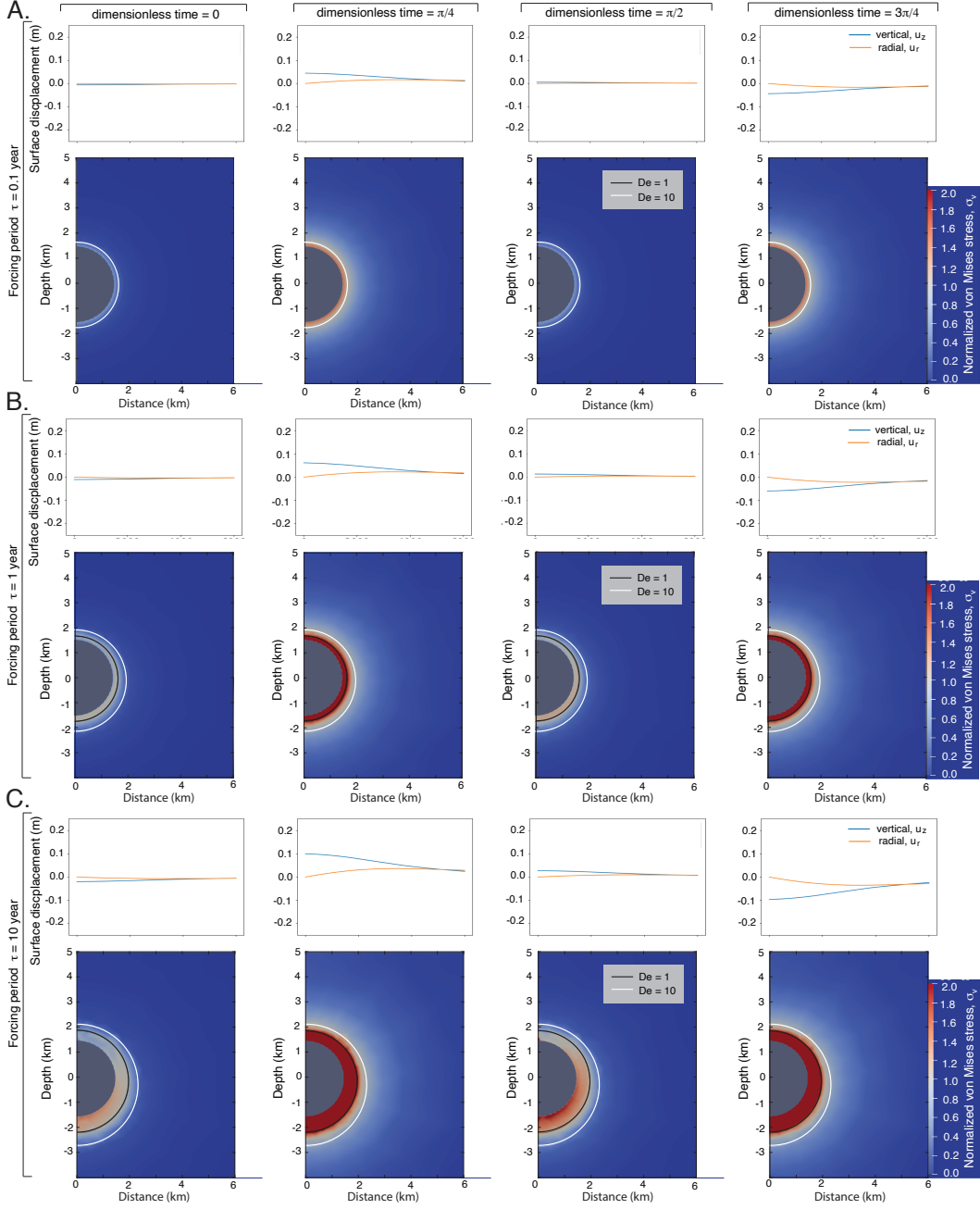


**Figure 6.** Spatial pattern of surface displacements  $u_z, u_r$  (top lines) and subsurface distribution of von Mises stress  $\sigma_v$  (bottom colors, normalized by  $P_0 = 10$  MPa) for dimensionless times  $0, \pi/4, \pi/2, 3\pi/4$  during a pressure cycle. Black contour is  $De = 1$ , white contour is  $De = 10$ , illustrating that a local Deborah number contour approximates the spatial region of elevated deviatoric stress and viscous strain around the chamber. **A.** Forcing period  $\tau = 0.1$  yr, max  $\sigma_v = 20.9$  MPa. **B.** Forcing period  $\tau = 1$  yr, max  $\sigma_v = 42.2$  MPa. **C.** Forcing period  $\tau = 10$  yr, max  $\sigma_v = 100.7$  MPa. Supplemental movies S1-S3 show time evolution of these simulations in more detail.

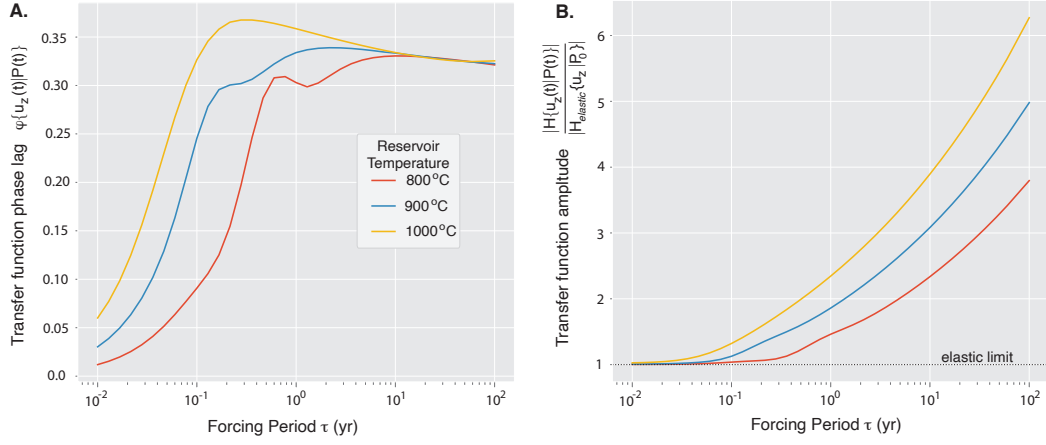


**Figure 7.** Transfer function between reservoir pressure and maximum vertical surface displacement  $H\{u_z(r=0, z=D+b, t)|P(t)\}$  as a function of sinusoidal pressure forcing period  $\tau$ . Colored curves correspond to different reservoir temperatures, each case assumes surface temperature  $T_s = 0^\circ\text{C}$  and geothermal gradient  $\alpha = 20\text{ C/km}$ . **A.** Phase lag  $\phi\{u_z(r=0, z=D+b, t)|P(t)\}$  (in radians). **B.** Amplitude  $|H\{u_z(r=0, z=D+b, t)|P(t)\}|$  normalized by the corresponding variable coefficient elastic case at each temperature. For the three reservoir temperatures explored here,  $|H_{elastic}\{u_z(r=0, z=D+b)|P_0\}| = 6.509 \times 10^{-9}, 6.822 \times 10^{-9}, 7.163 \times 10^{-9}$  m/Pa for  $T_c = 800, 900, 1000^\circ\text{C}$  respectively.

711 tem viscoelastic response. Most pronounced is a saturation of phase lag at  $\sim 0.3$  radi-  
 712 ans and muted amplification of displacements relative to the constant coefficient case.  
 713 As evidenced by the large  $\sigma_v$  (which measures deviatoric shear stress magnitude), vis-  
 714 cuous effects are confined near the reservoir wall. This results in more pronounced me-  
 715 chanical lag at the reservoir wall than at the surface (Figure 5) and concentration of shear  
 716 stress  $\sigma_v$  through the cycle in a narrow aureole around the chamber (Figure 6).

717 The strong spatial variability in material parameters now implies a spectrum of Maxwell  
 718 relaxation times as has been noted in other studies, (e.g., Head et al., 2021), and hence  
 719 spatially variable Deborah number. Nonetheless, we see that a local value of  $De$  still char-  
 720 acterizes the region experiencing significant viscous strain for each forcing period. Fig-  
 721 ure 6 shows that  $De \approx 10$  effectively bounds the region experiencing significant von Mises  
 722 stress, and hence viscous strain, in excess of chamber overpressure  $P_0$ , with  $De = 1$  once  
 723 again a measure of the viscous region centroid. For small forcing periods the viscous re-  
 724 gion is significantly reduced ( $De = 1$  does not appear for  $\tau = 0.1$  year forcing period).  
 725 Both contours are asymmetric with depth due to the geothermal gradient. To isolate vis-  
 726 cuous effects, the transfer amplitudes for Figure 7 are normalized using the variable co-  
 727 efficient elastic limit. That is, elastic parameters are computed using a thermal profile  
 728 but viscosity  $\eta = 1 \times 10^{34} \text{Pa} \cdot \text{s}$ . Then this variable coefficient elastic problem is simu-  
 729 lated and a transfer function  $H_{elastic}$  is computed from the output.

730 The transfer function curves in Figure 7 have more complex structure than their  
 731 constant coefficient counterpart in Figure 4. First, the phase lag  $\phi\{u_z(r = 0, z = D +$   
 732  $b, t) | P(t)\}$  is non-monotonic, with two local maxima superimposed on a sigmoidal in-  
 733 crease from 0 to  $\sim 0.3$  radians over three orders of magnitude in forcing period. The  
 734 second of these is a global maximum for the range of forcing periods we explored (100  
 735 years maximum), and appears to reflect the finite region around the chamber in which  
 736 viscous strains occur. Increasing the reservoir temperature from  $800^\circ\text{C}$  to  $1000^\circ\text{C}$  shifts  
 737 this global maximum as well as the sigmoidal uptick in phase lag to shorter periods, which  
 738 suggests that the local maxima are due in part to an expanded viscous shell around the  
 739 reservoir (i.e., larger region where  $De < 10$ ). As will be discussed in the next section,  
 740 we speculate that a non-monotonic phase lag at longer periods occurs because larger re-  
 741 gions of the domain begin to contribute to the surface displacements. We expect that  
 742 the shape of this phase lag curve as metric of viscoelastic response likely depends on spa-  
 743 tial rheologic structure, boundary conditions, and chamber geometry, although a param-  
 744 eter exploration is out of the scope of this study.

745 The apparent global maximum seen in the phase lag in Figure 7 is not mirrored  
 746 by the amplitude of displacements. Relative to the elastic limit transfer function ampli-



747 tude show a continuous increase in maximum displacements at increasing  $\tau$ , mirrored  
 748 by the spatial pattern of  $u_z$  and  $u_r$  in Figure 6. There is an inflection point that corre-  
 749 sponds to the local minimum in  $\phi$  for the lower reservoir temperatures, but viscous am-  
 750 plification is otherwise a monotonically increasing function of  $\tau$ , with amplification fac-  
 751 tors at 100 yr forcing period  $\sim 3.8\times$ ,  $\sim 5\times$  and  $\sim 6.3\times$  for  $800^\circ\text{C}$ ,  $900^\circ\text{C}$ , and  $1000^\circ\text{C}$  cham-  
 752 ber temperatures. At small  $\tau$  the amplification factor is asymptotic to the variable co-  
 753 efficient elastic limit (dashed line) in all cases.

## 754 **6 Discussion**

755 This work makes two primary contributions. First, we develop a rigorous numer-  
 756 ical framework based on a high-order finite element method for the computation of de-  
 757 formation and stress around axisymmetric magma reservoirs. Second, we study a par-  
 758 ticular problem - sinusoidal pressurization/depressurization of a spherical reservoir in  
 759 a half-space - and demonstrate how surface deformation patterns are frequency depen-  
 760 dent. This section is organized into a discussion associated with each contribution as they  
 761 relate to the phenomenology of viscoelastic deformation around volcanoes.

### 762 **6.1 Computational Considerations for Time-evolving Magmatic Systems**

763 Viscoelastic deformation of volcanoes has been studied analytically and numeri-  
 764 cally by numerous authors (e.g., Hickey & Gottsmann, 2014; Segall, 2019; Zhan & Gregg,  
 765 2019). However, we are unaware of a systematic analysis of the numerical and compu-  
 766 tational issues associated with this problem. As volcanic deformation datasets become  
 767 better resolved in space and time, and as magma reservoir models are generalized to in-  
 768 clude more physical processes over an increasing range of timescales, neglecting these nu-  
 769 merical and computational considerations is likely to be a major factor limiting scien-  
 770 tific progress.

771 We derived conditions on the time step, which guarantees stability of the aging law,  
 772 and showed that the numerical solution converges to the exact solution at the theoret-  
 773 ical rates of convergence in both space and time. However, in practice, even these 2D  
 774 simulations are computationally expensive because a system of equations (the discretized  
 775 equilibrium equation) must be solved at each time step, and this constitutes the bulk  
 776 of the computational load. We perform a direct solve of the system while it is still pos-  
 777 sible to hold the matrix factorization in system memory. For larger problems (e.g. in 3D  
 778 or with larger domains sizes or if a finer spatial resolution is required), matrix-free it-  
 779 erative methods on parallel machines would be necessary (Chen et al., 2022). Further-  
 780 more, if the relevant time scale of interest is the forcing period  $\tau$ , which can be much longer

781 than the minimum viscous relaxation time  $\eta/\mu$  (so that  $De \ll 1$ ), the problem can be  
 782 become arbitrarily numerically stiff: very small time steps are required for numerical sta-  
 783 bility, much smaller than that required to accurately resolve the sinusoidal pressure forc-  
 784 ing.

785 To address this corresponding computational burden, an implicit time stepping scheme  
 786 (such as backward Euler) would need to be applied, or alternative schemes such as split-  
 787 ting algorithms (Carcione & Quiroga-Goode, 1995). For problems in which total strains  
 788 are large (e.g., dominated by viscous flow) it may also be advantageous to reformulate  
 789 the governing equations in terms of split viscous and elastic strain rates (rather than strains),  
 790 as is commonly done in mantle dynamics models (e.g., Moresi et al., 2002). A disadvan-  
 791 tage of this approach is that elastic stresses are less explicitly resolved, which is not ac-  
 792 ceptable for the present application. Still, one drawback of our method is that it is not  
 793 robust in the incompressible limit ( $\nu = 0.5$ ). More sophisticated locking-free mixed fi-  
 794 nite element techniques (e.g., Gopalakrishnan and Guzmán (2012)) could be employed  
 795 to solve the equilibrium equations stably in the incompressible limit, a potential neces-  
 796 sity in fully coupled fluid-solid magmatic models. Codes developed for large-scale geo-  
 797 dynamic applications commonly include compressible fluid but incompressible solid me-  
 798 chanics (e.g., Heister et al., 2017). This difference in approach implies that extensions  
 799 of our computational framework to a broader range of problems might require further  
 800 numerical developments.

801 The inclusion of boundary tractions (to represent background tectonic stress, for  
 802 example) can be explored here directly by setting specific values of the boundary data.  
 803 Topography at the surface or at depth can be included by modifying the axisymmetric  
 804 domain geometry. Complex time-evolving forcing can be included so long as the high-  
 805 est frequency is resolved by the timestep, as we demonstrate in the next section. But highly  
 806 multiscale time evolution, such as might be expected for pressure at the reservoir wall  
 807 over eruption cycles (Cianetti et al., 2012), may require adaptive time-stepping techniques  
 808 to integrate efficiently through regions of both slow and fast evolution. Similar challenges  
 809 arise in the modeling of long-term earthquake cycles (e.g., Erickson & Dunham, 2014),  
 810 and similar timestepping approaches could be leveraged for simulating volcanic activ-  
 811 ity.

## 812 **6.2 Frequency Dependent Magmatic Deformation**

813 We have studied here a magma chamber problem that, while simplified in some re-  
 814 spects, has a strong basis in past observations and represents a template for future ad-  
 815 vances. In the elastic limit, corrections for less idealized geometry and material hetero-

816 geneity are known (Segall, 2010), and elastic parameter trade-offs have been explored  
 817 to some extent (e.g., Currenti & Williams, 2014; Rivalta et al., 2019). But viscoelastic  
 818 behavior is far less well understood. Case studies have demonstrated important trade-  
 819 offs in geometry, constitutive law, and thermal state, as well as complications associated  
 820 with time-dependent rheology (e.g., Grapenthin et al., 2010; Segall, 2019; Head et al.,  
 821 2019, 2021). But general time-dependence introduces significant complexities.

822 The cyclic forcing studied here represents a powerful framework to explore phenomenol-  
 823 ogy of transient magma chamber deformation. While magma pressure histories are not  
 824 generally sinusoidal, linear viscoelasticity (in any form, not just the Maxwell model) im-  
 825 plies that arbitrary forcing histories may be constructed through appropriate superpo-  
 826 sition. The analysis of section 4.2 details how knowledge of the transfer function can be  
 827 used to relate such composite signals. We illustrate this approach with three examples.

828 First, consider a reservoir pressure history (the input signal) given by the  $2\tau$ -periodic  
 829 rectangular pulse of unit width

$$830 \quad P(t) = P_0 (\mathcal{H}(t) - \mathcal{H}(t - 1)), \quad (74)$$

831 with  $\tau > 1$ . The complex Fourier series representation for  $P(t)$  can be expressed as

$$832 \quad P(t) = \sum_{n=-\infty}^{\infty} c_n e^{i\omega_n t}, \quad (75)$$

833 where  $\omega_n = n\pi/\tau$  and the complex Fourier coefficients are given by

$$834 \quad c_n = P_0 \frac{1}{\tau\omega_n} e^{-i\omega_n/2} \sin(\omega_n/2). \quad (76)$$

835 Then the output signal  $y(t)$  can be expressed in terms of its Fourier series

$$836 \quad y(t) = \sum_{n=-\infty}^{\infty} d_n e^{i\omega_n t} \quad (77)$$

837 with coefficients

$$838 \quad d_n = H(i\omega_n)c_n, \quad (78)$$

839 i.e. the coefficients of the input signal, scaled by the transfer function  $H$ . This exam-  
 840 ple demonstrates that sequences of impulsive pressure changes (such as eruptions) that  
 841 are non-harmonic in time can still be characterized with the framework developed here.

842 As a second example, if the pressure history is given by a unit impulse at  $t = t_0$ ,  
 843 namely

$$844 \quad P(t) = P_0 \delta(t - t_0), \quad (79)$$

845 then Equation 60 implies that the output signal is simply

$$846 \quad y(t) = h(t - t_0), \quad (80)$$

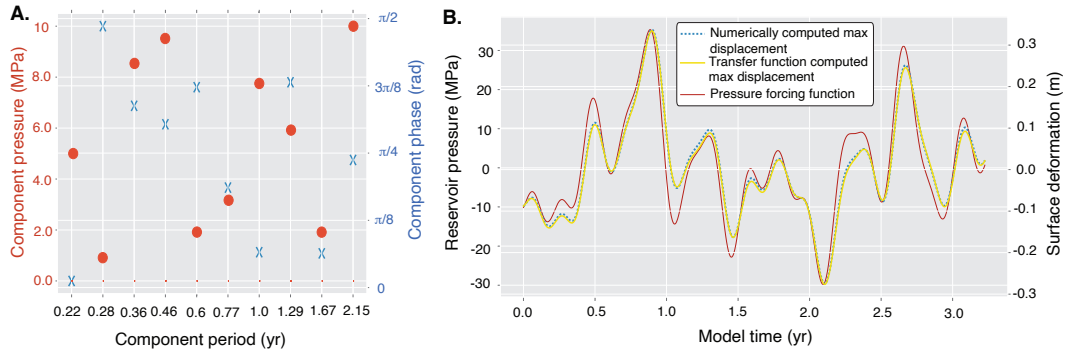


**Figure 8.** **A.** Amplitudes and phases of input pressure signal, Equation (69). **B.** Input pressure timeseries (red curve) along with numerically computed maximum surface displacement (dashed blue curve) and analytic prediction based on the transfer function, Equation 70.

847 i.e. the system impulse response. This pressure history represents a simple model for sud-  
 848 den pressure perturbation (e.g., Segall, 2016). The implied ground deformation in this  
 849 case is the impulse response function of the magma chamber/host rock system.

850 These examples demonstrate the transfer function approach in a forward model-  
 851 ing framework. Frequency-domain inversion of magmatic pressure histories from ground  
 852 motions, a common scenario since reservoir pressure is generally unknown, by extension  
 853 involves seeking weights for the forcing periods represented in Figure 7 to match gen-  
 854 eral time-dependent deformation data. To demonstrate this explicitly, we present a third  
 855 example in which we construct a non-harmonic input pressure signal by summing sinu-  
 856 soids at a subset of forcing frequencies explored in Figure 7 with random phase and am-  
 857 plitude (assuming an  $800^{\circ}\text{C}$  chamber representing a lower bound to the viscoelastic re-  
 858 sponse) corresponding to Equation 69. Weights and phases are displayed in Figure 8.A.  
 859 We compute the output signal from Equation 70 and show that the predicted surface  
 860 deformation matches the numerically computed output (Figure 8.B). Numerical displace-  
 861 ments shown here are after a spin-up to make sure the output is in steady state with the  
 862 input.

863 Outputs of interest are thus easily found given knowledge of the transfer function.  
 864 Of course, in reality this transfer function is unknown and would need to be computed  
 865 as part of an inversion. Further studies will be needed to quantify the variability of the  
 866 transfer function as control parameters are varied. This will determine the sensitivity  
 867 of phase lag and amplitude spectrum to rheologic model, chamber geometry, and tem-  
 868 perature structure.

869 Figure 8.B also demonstrates the non-trivial impact of frequency-dependent phase  
 870 lag and amplitude on ground deformation. Even though a relatively narrow range of fre-  
 871 quencies is present in the forcing function ( $2\pi/\omega_k = \tau_k \sim 0.2 - 2$  yr in equation 69),  
 872 we see that shorter period forcing generates in-phase ground displacements, while longer  
 873 period ground motions are out of phase with chamber pressure. These effects would be  
 874 amplified for warmer (more viscous) host rocks and longer forcing periods, and should  
 875 be observable in geodetic timeseries with several day resolution (phase lag associated with  
 876 1 year forcing period from Figure 7 is  $\sim 18$  days). We also see that the ground displace-  
 877 ment amplitude is a function of frequency as predicted from the transfer function. It is  
 878 not simply proportional to the pressure as would be expected from elasticity (Mogi, 1958),  
 879 and reflects the amplitudes of each component period shown in fig 8.A scaled by the trans-  
 880 fer function.

881 An interesting challenge implied by our analysis with respect to observations how-  
 882 ever is how to find initial conditions. Our time-dependent steady-state (purely oscilla-  
 883 tory) implicitly starts from a unstressed state, but as illustrated through 1D analysis (Sec-  
 884 tion 4) the initial strain determines the equilibrium position around which steady vis-  
 885 coelastic oscillations occur. In the 2D variable coefficients case the choice of initial strain  
 886 that will result in a particular chamber size (or geometry) is less trivially found - equi-  
 887 librium magma chamber volume is not an independent parameter but rather a model  
 888 outcome. From a geophysical perspective, this implies that absolute stress histories are  
 889 needed to interpret general surface displacement timeseries at volcanoes, and could play  
 890 an important role in eruption cycles as it does for earthquake cycles (e.g., Erickson et  
 891 al., 2017).

892 Another important implication of this model is that the volume of crustal rock around  
 893 the chamber that experiences viscous strain over a chamber pressure cycle depends on  
 894 the frequency of forcing. As demonstrated by Figure 4,  $De = 10$  effectively marks the  
 895 onset of viscous host response to cycling pressure forcing. Figure 6 extends this to vari-  
 896 able coefficients, suggesting that  $De \approx 10$  effectively bounds the region in which sig-  
 897 nificant deviatoric shear stresses (as measured by  $\sigma_v$  in excess of  $P_0$ ) occur.

898 We suggest that the frequency-dependent  $De \approx 10$  contour represents an effec-  
 899 tive outer edge to the viscoelastic “shell” at a given frequency of forcing. This shell has  
 900 been largely considered fixed in size by previous models for viscoelastic magma cham-  
 901 ber mechanics (e.g., Dragoni & Magnanensi, 1989; Jellinek & DePaolo, 2003; Karlstrom  
 902 et al., 2010; Degruyter & Huber, 2014; Segall, 2016; Liao et al., 2021). Our model demon-  
 903 strates that viscoelastic shell size even for a steady temperature distribution depends

904 on the time history of reservoir stress - like equilibrium reservoir size, it is a transient  
 905 model output.

### 906 **6.3 Implications for Transcrustal Magmatic Systems**

907 Magma reservoirs that feed volcanic eruptions likely sit near the top of transcrustal  
 908 magma transport networks characterized by high temperatures and partial melt (Sparks  
 909 et al., 2017). Some of this magma accumulates episodically into high melt fraction reser-  
 910 voirs such as we model here. But it is to be expected that, as transcrustal magma trans-  
 911 port networks mature, a significant fraction of the crust is heated and remains hot for  
 912 extended periods of time. What are the implications of this rheological structure for ground  
 913 deformation?

914 We can begin to answer this question by noting that the bulk crustal rheology of  
 915 magma storage zones as expressed by surface deformation depends on frequency of forc-  
 916 ing, as it does on the spatial structure of melt and temperature (Mullet & Segall, 2022).  
 917 This has been long recognized for crustal rheology in other settings (O’connell & Budi-  
 918 ansky, 1978; Lau & Holtzman, 2019). But volcanoes offer a particularly interesting case  
 919 for exploring crustal rheology, because different histories of heating – all else equal – will  
 920 have distinct deformation frequency response curves (transfer functions) in the frequency  
 921 band where geophysical observations are routinely made.

922 Figure 9 plots the  $De = 10$  contour representing onset of viscous mechanical re-  
 923 sponse for different pressurization periods, from 0.1 to 1000 years. We then consider end  
 924 member steady state thermal regimes: chamber boundary temperature of  $T_c = 800^\circ\text{C}$   
 925 and  $1200^\circ\text{C}$ , and geothermal gradient of  $\alpha = 20^\circ\text{C}/\text{km}$  and  $35^\circ\text{C}/\text{km}$ . In the cold ex-  
 926 treme (Figure 9A), we see that viscoelastic behavior is confined to a shell around the  
 927 chamber in all but 1000 year forcing. This is consistent with commonly used models of  
 928 isolated magma chambers. At long forcing periods however the mid/lower crust is ac-  
 929 tivated and starts to creep, defining a mid-crustal brittle-ductile transition that depends  
 930 on background geothermal gradient. In the hot extreme (Figure 9D), we see that vis-  
 931 coelastic response of the near-chamber region extends continuously into the mid-crust  
 932 for forcing periods as low as 10 years. This defines a spatially coherent viscous domain  
 933 induced by magmatic heating (Karlstrom et al., 2017), activated by long-period forcing.

934 While we leave further exploration of this to future work, we note that some of the  
 935 structure seen in phase lag variations in Figure 7 likely reflect changes to the shape as  
 936 well as volume of the viscous near-chamber region. It is notable that significant sensi-  
 937 tivity of viscoelastic response to forcing period and variations in thermal structure in the

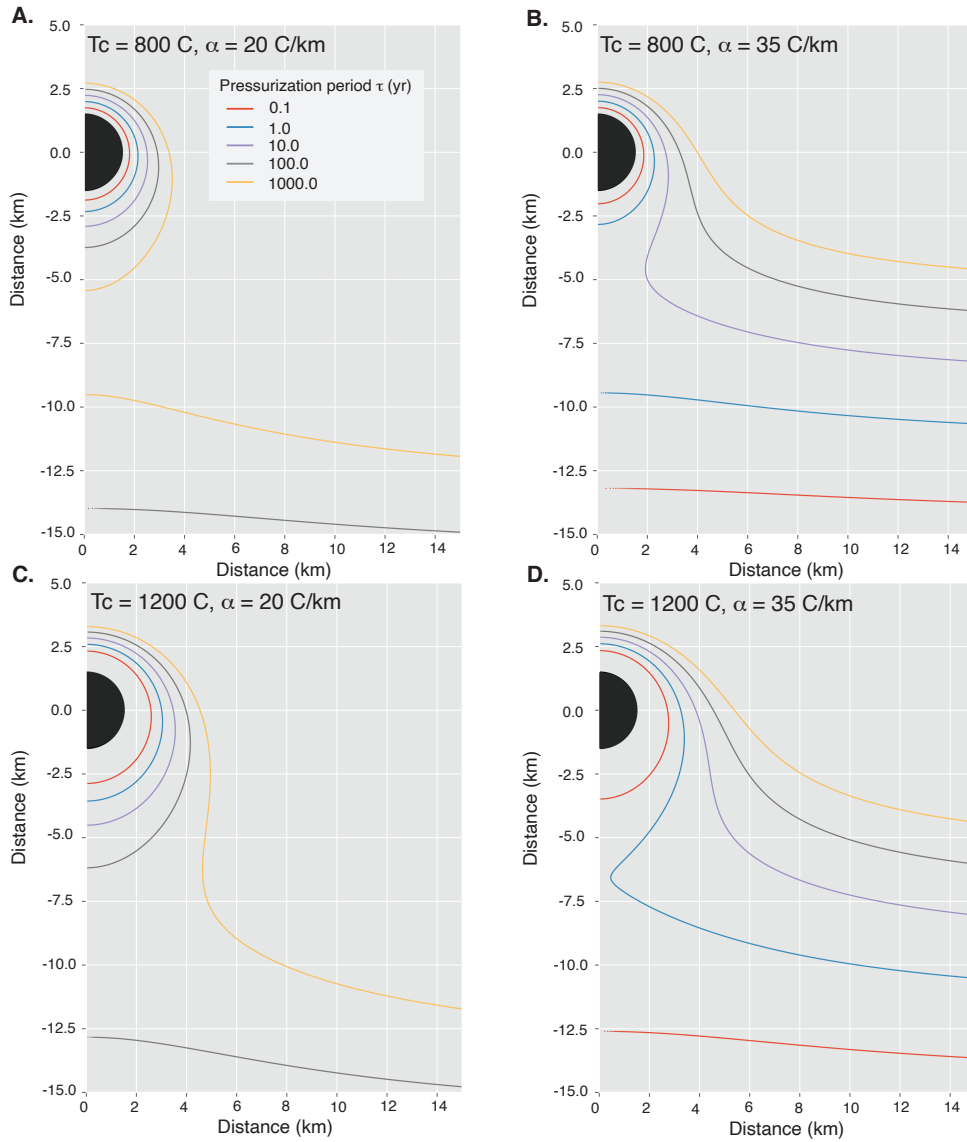


**Figure 9.** Spatial regions associated with a local Deborah number  $De = 10$  for varying periods  $\tau$  of the chamber pressure forcing function (colored curves), illustrating end member thermal regimes. Magma reservoir is black semi-circle in all panels. **A.** Reservoir temperature  $T_c = 800^\circ\text{C}$  with geothermal gradient  $\alpha = 20^\circ\text{C}/\text{km}$ . **B.** Reservoir temperature  $T_c = 800^\circ\text{C}$  with geothermal gradient  $\alpha = 35^\circ\text{C}/\text{km}$ . **C.** Reservoir temperature  $T_c = 1200^\circ\text{C}$  with geothermal gradient  $\alpha = 20^\circ\text{C}/\text{km}$ . **D.** Reservoir temperature  $T_c = 1200^\circ\text{C}$  with geothermal gradient  $\alpha = 35^\circ\text{C}/\text{km}$ .

938 0.1–10 year range, where geodetic observations are increasingly common. Because magma  
 939 transport is unsteady at many scales, ground deformation in volcanic regions will like-  
 940 wise include contributions from viscoelastic deformation defining the crustal thermo-rheologic  
 941 footprint of magmatism on a range of timescales.

## 942 **Appendix A Verification via Convergence Tests**

943 We verify the accuracy of our numerical method using the method of manufactured  
 944 solutions (MMS) (Roache, 1998) and explain this technique in the context of the dimen-  
 945 sional problem (computationally we solve the non-dimensionalized problem). The MMS  
 946 verification technique lets us choose arbitrary solution fields  $u^*(r, z, t), C^*(r, z, t)$  to act  
 947 as exact solutions to any initial-boundary-value problem, even those without a known  
 948 analytic solution) necessary for measuring convergence. The key point is that  $u^*$  and  $C^*$   
 949 satisfy the governing equations and boundary conditions with particular choices of source  
 950 terms and boundary data which we detail in this section.

951 We choose a manufactured solution to the initial-boundary-value problem Equa-  
 952 tion (1a),(4)-(8) based on the well-known solution to the pressurized magma cavity prob-  
 953 lem in an elastic half-space (Mogi, 1958; Segall, 2010) given by

$$954 \mathbf{u}_e = \frac{P_0 a^3}{4\mu(r^2 + z^2)^{3/2}} \begin{bmatrix} r \\ z \end{bmatrix}. \quad (\text{A1})$$

955 which satisfies the reservoir pressure conditions Equations (17a)-(17b). Define the man-  
 956 ufactured solutions  $u^*, C^*$  by

$$957 u^*(r, z, t) = (2 - e^{-t})\mathbf{u}_e, \quad (\text{A2})$$

$$958 C^*(r, z, t) = (1 - e^{-t})\mathbf{E}\underline{\underline{\epsilon}}(\mathbf{u}_e), \quad (\text{A3})$$

959 which satisfies equilibrium and specifies all boundary data. It does not however satisfy  
 960 the aging law, and to correct for this discrepancy a source term is added, namely

$$961 \dot{\underline{\underline{C}}} = \mathbf{E}\mathbf{A}\underline{\underline{\sigma}} + \mathbf{G}. \quad (\text{A4})$$

962 Here, the source term  $\mathbf{G}$  is determined from the manufactured solutions to be

$$963 \mathbf{G} = e^{-t}\sigma^* - \frac{\mu}{\eta} \text{dev } \sigma^*, \quad (\text{A5})$$

964 where  $\sigma^*$  is the manufactured stress and can be obtained by computing

$$965 \sigma^* = \mathbf{E}\underline{\underline{\epsilon}}(\mathbf{u}_e). \quad (\text{A6})$$

966 All parameters used are given in Table A1. Table A2 shows the spatial errors  $\|\underline{\underline{C}} - \underline{\underline{C}}_h\|$   
 967 and  $\|\mathbf{u} - \mathbf{u}_h\|$  when computing approximations to  $C^*$  and  $u^*$  after a single time step, us-  
 968 ing a stable step size of  $10^{-7}$  and the discrete  $L^2$ -norm. Successive mesh refinements are



**Table A1.** Parameters used in Convergence Tests and their Symbols.

Symbol	Explanation	Value
$a$	Ellipse semi-major axis	4 km
$b$	Ellipse semi-minor axis	4 km
$D$	Reservoir depth beneath Earth's surface	5 km
$L_r$	Domain length	10 km
$L_z$	Domain depth	10 km
$\mu$	shear modulus	0.5 GPa
$\lambda$	Lamé's first parameter	4 GPa
$\eta$	Viscosity	0.5 GPa-s
$P_0$	Chamber Pressure	10 MPa

**Table A2.** Spatial convergence data, measured with respect to the discrete  $L^2$ -norm, for a single time step of  $\Delta t = 10^{-7}$  using polynomials of degree 3.

$h$	$\ \underline{\mathbf{C}} - \underline{\mathbf{C}}_h\ $	$\underline{\mathbf{C}}$ -rate	$\ \mathbf{u} - \mathbf{u}_h\ $	$\mathbf{u}$ -rate
$h/2$	$5.25 \times 10^{-9}$		$1.84 \times 10^{-8}$	
$h/4$	$7.17 \times 10^{-10}$	2.87	$1.31 \times 10^{-9}$	3.81
$h/8$	$9.13 \times 10^{-11}$	2.97	$8.41 \times 10^{-11}$	3.96
$h/16$	$1.14 \times 10^{-11}$	3.00	$5.24 \times 10^{-12}$	4.00

**Table A3.** Temporal convergence data measured at point  $(\tilde{A}, 0)$  under the discrete  $L^2$ -norm.

$\Delta t$	$\ \underline{C} - \underline{C}_h\ $	$\underline{C}$ -rate	$\ \mathbf{u} - \mathbf{u}_h\ $	$\mathbf{u}$ -rate
$\Delta t/2$	$1.75 \times 10^{-1}$		$1.18 \times 10^{-6}$	
$\Delta t/4$	$8.85 \times 10^{-2}$	0.99	$5.96 \times 10^{-7}$	0.99
$\Delta t/8$	$4.46 \times 10^{-2}$	0.99	$3.01 \times 10^{-7}$	0.99

969 made using polynomials of degree 3 as a basis for the FEM space. Convergence rates agrees  
 970 with FEM theory which predict a convergence rate of  $p + 1$  for  $u^*$  and  $p$  for  $C^*$  when  
 971 polynomials of degree  $p$  are used (Larsson & Thomée, 2008). The same convergence pat-  
 972 tern is observed for polynomials with degree greater than 3 except that the  $L^2$ -error drops  
 973 below machine precision leading to round-off error in the rate computation.

974 To measure the convergence in the temporal domain we select a single point in space  
 975 and perform successive mesh refinements in time. Table A3 shows that both  $\underline{C}$  and  $\mathbf{u}$   
 976 exhibit rate-1 temporal convergence, consistent with forward Euler.

977 The benefit of convergence tests based on the MMS technique is that solutions can  
 978 be manufactured for problems with more physical complexities, as opposed to relying  
 979 on simple problems with known analytic solutions such as those highlighted in (Hickey  
 980 & Gottsmann, 2014). With MMS, rigorous convergence can be obtained at the exact the-  
 981 oretical rate, a desirable outcome for high-order numerical methods. That being said,  
 982 the MMS technique requires making specific choices for source and boundary data, which  
 983 can sometimes alter the underlying physics of interest. Thus code verification can ben-  
 984 efit further from community based efforts, as done extensively in the earthquake com-  
 985 munity (Harris et al., 2009; Erickson et al., 2020). In community benchmarking, all math-  
 986 ematical details of a problem are specified and different modeling groups compare code  
 987 output and seek quantitative comparisons. These exercises can be done for problems with  
 988 or without a known analytic solution; the simple problems detailed in (Hickey & Gotts-  
 989 mann, 2014) (including the homogeneous, viscoelastic “Del Negro” model, (Del Negro  
 990 et al., 2009)) could serve as the first benchmark problem statements for the magma reser-  
 991 voir community code verification efforts, with further benchmark problems containing  
 992 increasingly physical and/or geometrical properties where analytic solutions are not known.

## 993 Open Research

994 Software consists of Python code developed on top of the free and open source multi-  
 995 physics library NGSolve (Schöberl, 2010–2022) and the accompanying mesh generator (Schöberl,

1996 1997). All source code is freely available in the public repository (*Bitbucket: magmaxisym*,  
1997 2022).

## 1998 Acknowledgments

1999 CR, BAE and LK were supported by NSF grant EAR- 2036980. LK also acknowl-  
1000 edges NSF grant 1848554. BL and JG were supported by NSF grant DMS-1912779. This  
1001 work benefited from access to the University of Oregon high performance computer Ta-  
1002 lapas and the COEUS cluster at the Portland Institute for Computational Science. We  
1003 thank James Hickey, an anonymous reviewer, and the editor for comments and sugges-  
1004 tions that improved the paper considerably. The authors acknowledge useful discussions  
1005 with Yang Liao and Ben Holtzman.

## 1006 References

- 1007 Allison, K. L., & Dunham, E. M. (2018). Earthquake cycle simulations with rate-  
1008 and-state friction and power-law viscoelasticity. *Tectonophysics*, *733*, 232–256.  
1009 doi: <https://doi.org/10.1016/j.tecto.2017.10.021>
- 1010 Anderson, K. A., & Segall, P. (2011). Physics-based models of ground deforma-  
1011 tion and extrusion rate at effusively erupting volcanoes. *Journal of Geo-*  
1012 *physical Research Solid Earth*, *116*(B7), 1–20. doi: [https://doi.org/10.1029/](https://doi.org/10.1029/2010JB007939)  
1013 [2010JB007939](https://doi.org/10.1029/2010JB007939)
- 1014 Bakker, R. R., Frehner, M., & Lupi, M. (2016). How temperature-dependent elas-  
1015 ticity alters host rock/magmatic reservoir models: A case study on the effects  
1016 of ice-cap unloading on shallow volcanic systems. *Earth and Planetary Science*  
1017 *Letters*, *456*, 16–25. doi: <https://doi.org/10.1016/j.epsl.2016.09.039>
- 1018 Berrino, G., Corrado, G., Luongo, G., & Toro, B. (1984). Ground deformation  
1019 and gravity changes accompanying the 1982 Pozzuoli uplift. *Bulletin vol-*  
1020 *canologique*, *47*(2), 187–200. doi: <https://doi.org/10.1007/BF01961548>
- 1021 *Bitbucket: magmaxisym*. (2022). [https://bitbucket.org/jayggg/magmaxisym/](https://bitbucket.org/jayggg/magmaxisym/src/master/)  
1022 [src/master/](https://bitbucket.org/jayggg/magmaxisym/src/master/). (Repository with python drivers for computing dynamics of vis-  
1023 coelastic medium surrounding an axisymmetric magma cavity.)
- 1024 Black, B. A., & Manga, M. (2017). Volatiles and the tempo of flood basalt magma-  
1025 tism. *Earth and Planetary Science Letters*, *458*, 130–140. doi: [https://doi.org/](https://doi.org/10.1016/j.epsl.2016.09.035)  
1026 [10.1016/j.epsl.2016.09.035](https://doi.org/10.1016/j.epsl.2016.09.035)
- 1027 Bonafede, M., Dragoni, M., & Quarenì, F. (1986). Displacement and stress fields  
1028 produced by a centre of dilation and by a pressure source in a viscoelastic half-  
1029 space: application to the study of ground deformation and seismic activity at

- 1030 Campi Flegrei, Italy. *Geophysical Journal International*, 87(2), 455–485. doi:  
 1031 <https://doi.org/10.1111/j.1365-246X.1986.tb06632.x>
- 1032 Bürgmann, R., & Dresen, G. (2008). Rheology of the lower crust and upper mantle:  
 1033 Evidence from rock mechanics, geodesy, and field observations. *Annual Review*  
 1034 *of Earth and Planetary Sciences*, 36, 531–567. doi: [https://doi.org/10.1146/](https://doi.org/10.1146/annurev.earth.36.031207.124326)  
 1035 [annurev.earth.36.031207.124326](https://doi.org/10.1146/annurev.earth.36.031207.124326)
- 1036 Carcione, J. M., & Quiroga-Goode, G. (1995). Some aspects of the physics and  
 1037 numerical modeling of biot compressional waves. *Journal of Computational*  
 1038 *Acoustics*, 03(04), 261-280. doi: <https://doi.org/10.1142/S0218396X95000136>
- 1039 Chen, A., Erickson, B., & Kozdon, J. (2022). Matrix-free methods for summation-  
 1040 by-parts finite difference operators on GPUs. *submitted*.
- 1041 Cianetti, S., Giunchi, C., & Casarotti, E. (2012). Volcanic deformation and  
 1042 flank instability due to magmatic sources and frictional rheology: the case  
 1043 of mount etna. *Geophysical Journal International*, 191, 939–953. doi:  
 1044 <https://doi.org/10.1111/j.1365-246X.2012.05689.x>
- 1045 Crozier, J., & Karlstrom, L. (2022). Evolving magma temperature and volatile  
 1046 contents over the 2008–2018 summit eruption of kīlauea volcano. *Science Ad-*  
 1047 *vances*, 8(22), eabm4310. Retrieved from [https://www.science.org/doi/](https://www.science.org/doi/abs/10.1126/sciadv.abm4310)  
 1048 [abs/10.1126/sciadv.abm4310](https://www.science.org/doi/abs/10.1126/sciadv.abm4310) doi: <https://doi.org/10.1126/sciadv.abm4310>
- 1049 Currenti, G., & Williams, C. A. (2014). Numerical modeling of deformation and  
 1050 stress fields around a magma chamber: Constraints on failure conditions and  
 1051 rheology. *Physics of the Earth and Planetary Interiors*, 226, 14–27. doi:  
 1052 <https://doi.org/10.1016/j.pepi.2013.11.003>
- 1053 Degruyter, W., & Huber, C. (2014). A model for eruption frequency of upper crustal  
 1054 silicic magma chambers. *Earth and Planetary Science Letters*, 403, 117–130.  
 1055 doi: <https://doi.org/10.1016/j.epsl.2014.06.047>
- 1056 Del Negro, C., Currenti, G., & Scandura, D. (2009). Temperature-dependent vis-  
 1057 coelastic modeling of ground deformation: Application to Etna volcano during  
 1058 the 1993–1997 inflation period. *Physics of the Earth and Planetary Interiors*,  
 1059 *172*(3), 299-309. doi: <https://doi.org/10.1016/j.pepi.2008.10.019>
- 1060 Dragoni, M., & Magnanensi, C. (1989). Displacement and stress produced by a pres-  
 1061 surized, spherical magma chamber, surrounded by a viscoelastic shell. *Physics*  
 1062 *of the Earth and Planetary Interiors*, 56(3), 316-328. doi: [https://doi.org/10](https://doi.org/10.1016/0031-9201(89)90166-0)  
 1063 [.1016/0031-9201\(89\)90166-0](https://doi.org/10.1016/0031-9201(89)90166-0)
- 1064 Erickson, B. A., & Dunham, E. M. (2014). An efficient numerical method for  
 1065 earthquake cycles in heterogeneous media: Alternating subbasin and surface-  
 1066 rupturing events on faults crossing a sedimentary basin. *Journal of Geophys-*

- 1067            *ical Research: Solid Earth*, 119(4), 3290-3316.    doi: <https://doi.org/10.1002/>  
1068            2013JB010614
- 1069    Erickson, B. A., Dunham, E. M., & Khosravifar, A.    (2017).    A finite difference  
1070            method for off-fault plasticity throughout the earthquake cycle. *Journal of the*  
1071            *Mechanics and Physics of Solids*, 109, 50-77.    doi: <https://doi.org/10.1016/>  
1072            j.jmps.2017.08.002
- 1073    Erickson, B. A., Jiang, J., Barall, M., Lapusta, N., Dunham, E. M., Harris, R., ...  
1074            Wei, M.    (2020).    The community code verification exercise for simulating se-  
1075            quences of earthquakes and aseismic slip (seas). *Seismological Research Letters*,  
1076            91, 874–890. doi: <https://doi.org/10.1785/0220190248>
- 1077    Ern, A., & Guermond, J.-L. (2021). *Finite elements i*. Springer.
- 1078    Golden, J., & Graham, G. (1988). *Boundary value problems in linear viscoelasticity*  
1079            (1st ed.). Springer-Verlag. doi: <https://doi.org/10.1137/1031072>
- 1080    Gopalakrishnan, J., & Guzmán, J. (2012). A second elasticity element using the ma-  
1081            trix bubble. *IMA J. Numer. Anal.*, 32, 352-372. doi: <https://doi.org/10.1093/>  
1082            imanum/drq047
- 1083    Gopalakrishnan, J., & Pasciak, J. E.    (2006).    The convergence of V-cycle multi-  
1084            grid algorithms for axisymmetric Laplace and Maxwell equations. *Mathemat-*  
1085            *ics of Computation*, 75, 1697–1719.    doi: <https://doi.org/10.1090/S0025-5718>  
1086            -06-01884-9
- 1087    Gottsmann, J., & Odbert, H.    (2014).    The effects of thermomechanical hetero-  
1088            geneities in island arc crust on time-dependent preeruptive stresses and the  
1089            failure of an andesitic reservoir. *Journal of Geophysical Research: Solid Earth*,  
1090            119, 4626–4639. doi: <https://doi.org/10.1002/2014JB011079>
- 1091    Grapenthin, R., Ófeigsson, B. G., Sigmundsson, F., Sturkell, E., & Hooper, A.  
1092            (2010).    Pressure sources versus surface loads: Analyzing volcano deformation  
1093            signal composition with an application to hekla volcano, iceland. *Geophysical*  
1094            *Research Letters*, 37(20). doi: <https://doi.org/10.1029/2010GL044590>
- 1095    Gregg, P., De Silva, S., & Grosfils, E. (2013). Thermomechanics of shallow magma  
1096            chamber pressurization: Implications for the assessment of ground deformation  
1097            data at active volcanoes. *Earth and Planetary Science Letters*, 384, 100–108.  
1098            doi: <https://doi.org/10.1016/j.epsl.2013.09.040>
- 1099    Gregg, P., De Silva, S., Grosfils, E., & Parmigiani, J.    (2012).    Catastrophic  
1100            caldera-forming eruptions: Thermomechanics and implications for eruption  
1101            triggering and maximum caldera dimensions on earth. *Journal of Volcanol-*  
1102            *ogy and Geothermal Research*, 241, 1–12.    doi: <https://doi.org/10.1016/>  
1103            j.jvolgeores.2012.06.009

- 1104 Harris, R. A., Barall, M., Archuleta, R., Dunham, E. M., Aagaard, B., Ampuero,  
1105 J. P., ... Templeton, E. (2009). The SCEC/USGS dynamic earthquake rupture  
1106 code verification exercise. *Seismological Research Letters*, *80*, 119–126. doi:  
1107 <https://doi.org/10.1785/gssrl.80.1.119>
- 1108 Head, M., Hickey, J., Gottsmann, J., & Fournier, N. (2019). The influence of vis-  
1109 coelastic crustal rheologies on volcanic ground deformation: Insights from  
1110 models of pressure and volume change. *Journal of Geophysical Research: Solid  
1111 Earth*, *124*(8), 8127–8146. doi: <https://doi.org/10.1029/2019JB017832>
- 1112 Head, M., Hickey, J., Gottsmann, J., & Fournier, N. (2021). Exploring the impact of  
1113 thermally controlled crustal viscosity on volcanic ground deformation. *Journal  
1114 of Geophysical Research: Solid Earth*, *126*(8), e2020JB020724. doi: [https://doi  
1115 .org/10.1029/2020JB020724](https://doi.org/10.1029/2020JB020724)
- 1116 Heister, T., Dannberg, J., Gassmüller, R., & Bangerth, W. (2017). High accuracy  
1117 mantle convection simulation through modern numerical methods. II: Realistic  
1118 models and problems. *Geophysical Journal International*, *210*(2), 833–851. doi:  
1119 <https://doi.org/10.1093/gji/ggx195>
- 1120 Henderson, S. T., & Pritchard, M. E. (2017). Time-dependent deformation of  
1121 Uturuncu volcano, Bolivia, constrained by GPS and InSAR measurements  
1122 and implications for source models. *Geosphere*, *13*(6), 1834–1854. doi:  
1123 <https://doi.org/10.1130/GES01203.1>
- 1124 Hickey, J., & Gottsmann, J. (2014). Benchmarking and developing numerical finite  
1125 element models of volcanic deformation. *Journal of Volcanology and Geother-  
1126 mal Research*, *280*, 126–130. doi: [https://doi.org/10.1016/j.jvolgeores.2014.05  
1127 .011](https://doi.org/10.1016/j.jvolgeores.2014.05)
- 1128 Hickey, J., Gottsmann, J., & Mothes, P. (2015). Estimating volcanic deformation  
1129 source parameters with a finite element inversion: The 2001–2002 unrest at co-  
1130 topaxi volcano, ecuador. *Journal of Geophysical Research: Solid Earth*, *120*(3),  
1131 1473–1486. doi: <https://doi.org/10.1002/2014JB011731>
- 1132 Huber, C., Townsend, M., Degruyter, W., & Bachmann, O. (2019). Optimal depth  
1133 of subvolcanic magma chamber growth controlled by volatiles and crust rhe-  
1134 ology. *Nature Geoscience*, *12*(9), 762–768. doi: [https://doi.org/10.1038/  
1135 s41561-019-0415-6](https://doi.org/10.1038/s41561-019-0415-6)
- 1136 Jellinek, A. M., & DePaolo, D. J. (2003). A model for the origin of large silicic  
1137 magma chambers: precursors of caldera-forming eruptions. *Bulletin of Vol-  
1138 canology*, *65*(5), 363–381. doi: <https://doi.org/10.1007/s00445-003-0277-y>
- 1139 Karakas, O., Degruyter, W., Bachmann, O., & Dufek, J. (2017). Lifetime and size  
1140 of shallow magma bodies controlled by crustal-scale magmatism. *Nature Geo-*

- 1141 *science*, 10(6), 446–450. doi: <https://doi.org/10.1038/ngeo2959>
- 1142 Karlstrom, L., Dufek, J., & Manga, M. (2010). Magma chamber stability in arc and  
1143 continental crust. *Journal of Volcanology and Geothermal Research*, 190(3),  
1144 249–270. doi: <https://doi.org/10.1016/j.jvolgeores.2009.10.003>
- 1145 Karlstrom, L., Paterson, S. R., & Jellinek, A. M. (2017). A reverse energy cascade  
1146 for crustal magma transport. *Nature Geoscience*, 10(8), 604–608. doi: <https://doi.org/10.1038/ngeo2982>
- 1147
- 1148 Larsson, S., & Thomée, V. (2008). *Partial differential equations with numerical*  
1149 *methods* (Vol. 45). Springer Science & Business Media. doi: [https://doi.org/10](https://doi.org/10.1007/978-3-540-88706-5)  
1150 [.1007/978-3-540-88706-5](https://doi.org/10.1007/978-3-540-88706-5)
- 1151 Lau, H. C., & Holtzman, B. K. (2019). “Measures of dissipation in viscoelastic  
1152 media” extended: Toward continuous characterization across very broad geo-  
1153 physical time scales. *Geophysical Research Letters*, 46(16), 9544–9553. doi:  
1154 <https://doi.org/10.1029/2019GL083529>
- 1155 Lau, H. C., Holtzman, B. K., & Havlin, C. (2020). Toward a self-consistent char-  
1156 acterization of lithospheric plates using full-spectrum viscoelasticity. *AGU Ad-*  
1157 *vances*, 1(4), e2020AV000205. doi: <https://doi.org/10.1029/2020AV000205>
- 1158 Le Mével, H., Gregg, P., & Feigl, K. (2016). Magma injection into a long-lived  
1159 reservoir to explain geodetically measured uplift: Application to the 2007-2014  
1160 unrest episode at Laguna del Maule volcanic field, Chile. *Journal of Geophys-*  
1161 *ical Research: Solid Earth*, 121, 6092–6108. doi: [https://doi.org/10.1002/](https://doi.org/10.1002/2016JB013066)  
1162 [2016JB013066](https://doi.org/10.1002/2016JB013066)
- 1163 Liao, Y., Soule, S. A., Jones, M., & Le Mével, H. (2021). The mechanical response of  
1164 a magma chamber with poroviscoelastic crystal mush. *Journal of Geophysical*  
1165 *Research: Solid Earth*, 126(4), e2020JB019395. doi: [https://doi.org/10.1029/](https://doi.org/10.1029/2020JB019395)  
1166 [2020JB019395](https://doi.org/10.1029/2020JB019395)
- 1167 Masterlark, T., Haney, M., Dickinson, H., Fournier, T., & Searcy, C. (2010). Rhe-  
1168 ologic and structural controls on the deformation of okmok volcano, alaska:  
1169 Fems, insar, and ambient noise tomography. *Journal of Geophysical Research:*  
1170 *Solid Earth*, 115, 1–22. doi: <https://doi.org/10.1029/2009JB006324>
- 1171 McTigue, D. F. (1987). Elastic stress and deformation near a finite spherical magma  
1172 body: resolution of the point source paradox. *Journal of Geophysical Re-*  
1173 *search: Solid Earth*, 92(B12), 12931–12940. doi: [https://doi.org/10.1029/](https://doi.org/10.1029/JB092iB12p12931)  
1174 [JB092iB12p12931](https://doi.org/10.1029/JB092iB12p12931)
- 1175 Mittal, T., & Richards, M. A. (2019). Volatile degassing from magma chambers as  
1176 a control on volcanic eruptions. *Journal of Geophysical Research Solid Earth*,  
1177 124(9), 7869–7901. doi: <https://doi.org/10.1029/2018JB016983>

- 1178 Mogi, K. (1958). Relations between the eruptions of various volcanoes and the de-  
 1179 formations of the ground surfaces around them. *Bulletin of the Earthquake Re-*  
 1180 *search Institute*, 36, 99–134.
- 1181 Morales Rivera, A. M., Amelung, F., Albino, F., & Gregg, P. M. (2019). Impact of  
 1182 crustal rheology on temperature-dependent viscoelastic models of volcano  
 1183 deformation: Application to Taal Volcano, Philippines. *Journal of Geo-*  
 1184 *physical Research: Solid Earth*, 115, 978–994. doi: [https://doi.org/10.1029/](https://doi.org/10.1029/2018JB016054)  
 1185 2018JB016054
- 1186 Moresi, L., Dufour, F., & Mühlhaus, H.-B. (2002). Mantle convection model-  
 1187 ing with viscoelastic/brittle lithosphere: Numerical methodology and plate  
 1188 tectonic modeling. *Pure and applied Geophysics*, 159(10), 2335–2356. doi:  
 1189 <https://doi.org/10.1007/s00024-002-8738-3>
- 1190 Muki, R., & Sternberg, E. (1961, 06). On Transient Thermal Stresses in Viscoelas-  
 1191 tic Materials With Temperature-Dependent Properties. *Journal of Applied Me-*  
 1192 *chanics*, 28(2), 193–207. doi: <https://doi.org/10.1115/1.3641651>
- 1193 Mullet, B., & Segall, P. (2022). The surface deformation signature of a transcrustal,  
 1194 crystal mush-dominant magma system. *Journal of Geophysical Research: Solid*  
 1195 *Earth*, 127(5), e2022JB024178. doi: <https://doi.org/10.1029/2022JB024178>
- 1196 Newman, A., Dixon, T. H., Ofoegbu, G., & Dixon, J. E. (2001). Geodetic and seis-  
 1197 mic constraints on recent activity at long valley caldera, california: evidence  
 1198 for viscoelastic rheology. *Journal of Volcanology and Geothermal Research*,  
 1199 105(3), 183–206. doi: [https://doi.org/10.1016/S0377-0273\(00\)00255-9](https://doi.org/10.1016/S0377-0273(00)00255-9)
- 1200 Novoa, C., Remy, D., Gerbault, M., Baez, J., Tassara, A., Cordova, L., ... Del-  
 1201 gado, F. (2019). Viscoelastic relaxation: A mechanism to explain the  
 1202 decennial large surface displacements at the Laguna del Maule silicic vol-  
 1203 canic complex. *Earth and Planetary Science Letters*, 521, 46–59. doi:  
 1204 <https://doi.org/10.1016/j.epsl.2019.06.005>
- 1205 O'connell, R., & Budiansky, B. (1978). Measures of dissipation in viscoelastic me-  
 1206 dia. *Geophysical Research Letters*, 5(1), 5–8. doi: [https://doi.org/10.1029/](https://doi.org/10.1029/GL005i001p00005)  
 1207 GL005i001p00005
- 1208 Rivalta, E., Corbi, F., Passarelli, L., Acocella, V., Davis, T., & Di Vito, M. A.  
 1209 (2019). Stress inversions to forecast magma pathways and eruptive vent lo-  
 1210 cation. *Science advances*, 5(7), eaau9784. doi: [https://doi.org/10.1126/](https://doi.org/10.1126/sciadv.aau9784)  
 1211 sciadv.aau9784
- 1212 Roache, P. J. (1998). *Verification and validation in computational science and engi-*  
 1213 *neering* (Vol. 895). Hermosa Albuquerque, NM.



- 1214 Schetzen, M. (2003). *Linear time-invariant systems* (1st ed.). The Institute of Elec-  
1215 trical and Electronics Engineers.
- 1216 Schöberl, J. (1997). NETGEN an advancing front 2D/3D-mesh generator based  
1217 on abstract rules. *Computing and Visualization in Science*, *1*(1), 41–52. doi:  
1218 <https://doi.org/10.1007/S007910050004>
- 1219 Schöberl, J. (2010–2022). *NGSolve*. <http://ngsolve.org>.
- 1220 Segall, P. (2010). *Earthquake and volcano deformation*. Princeton University Press.  
1221 doi: <https://doi.org/10.1515/9781400833856>
- 1222 Segall, P. (2016). Repressurization following eruption from a magma chamber with  
1223 a viscoelastic aureole. *Journal of Geophysical Research: Solid Earth*, *121*(12),  
1224 8501–8522. doi: <https://doi.org/10.1002/2016JB013597>
- 1225 Segall, P. (2019). Magma chambers: what we can, and cannot, learn from volcano  
1226 geodesy. *Philosophical Transactions of the Royal Society A*, *377*(2139). doi:  
1227 <https://doi.org/10.1098/rsta.2018.0158>
- 1228 Sigmundsson, F., Pinel, V., Lund, B., Albino, F., Pagli, C., Geirsson, H., & Sturkell,  
1229 E. (2010). Climate effects on volcanism: influence on magmatic systems  
1230 of loading and unloading from ice mass variations, with examples from Ice-  
1231 land. *Philosophical Transactions of the Royal Society A*, *368*(1919). doi:  
1232 <https://doi.org/10.1098/rsta.2010.0042>
- 1233 Sparks, R. S. J., Cashman, K., & Calais, E. (2017). Dynamic magma systems:  
1234 Implications for forecasting volcanic activity. *Elements*, *13*(1), 35–40. doi:  
1235 <https://doi.org/10.2113/gselements.13.1.35>
- 1236 Townsend, M. (2022). Linking surface deformation to thermal and mechanical  
1237 magma chamber processes. *Earth and Planetary Science Letters*, *577*, 117–272.  
1238 doi: <https://doi.org/10.1016/j.epsl.2021.117272>
- 1239 Townsend, M., Huber, C., Degruyter, W., & Bachmann, O. (2019). Magma cham-  
1240 ber growth during intercaldera periods: Insights from thermo-mechanical  
1241 modeling with applications to Laguna del Maule, Campi Flegrei, Santorini,  
1242 and Aso. *Geochemistry, Geophysics, Geosystems*, *20*(3), 1574–1591. doi:  
1243 <https://doi.org/10.1029/2018GC008103>
- 1244 Walwer, D., Ghil, M., & Calais, E. (2021). Oscillatory nature of the Okmok vol-  
1245 cano’s deformation. *Philosophical Transactions of the Royal Society A*, *506*,  
1246 76–86. doi: <https://doi.org/10.1016/j.epsl.2018.10.033>
- 1247 Yamasaki, T., Kobayashi, T., Wright, T., & Fukahata, Y. (2018). Viscoelastic  
1248 crustal deformation by magmatic intrusion: A case study in the Kutcharo  
1249 caldera, eastern Hokkaido, Japan. *Journal of Volcanology and Geothermal*  
1250 *Research*, *349*, 128–145. doi: <https://doi.org/10.1016/j.jvolgeores.2017.10.011>

- 1251 Zhan, Y., & Gregg, P. (2019). How accurately can we model magma reservoir fail-  
1252 ure with uncertainties in host rock rheology? *Journal of Geophysical Research:*  
1253 *Solid Earth*, *124*(8), 8030–8042. doi: <https://doi.org/10.1029/2019JB018178>
- 1254 Zhong, X., Dabrowski, M., & Jamtveit, B. (2019). Analytical solution for the stress  
1255 field in elastic half-space with a spherical pressurized cavity or inclusion con-  
1256 taining eigenstrain. *Geophysical Journal International*, *216*(2), 1100–1115. doi:  
1257 <https://doi.org/10.1093/gji/ggy447>